UNIVERSIDADE DE SÃO PAULO
ESCOLA DE ENGENHARIA DE SÃO CARLOS

Sergio Sesé Ballester

General Analysis of a Hybrid Rocket Model using CFD

São Carlos

2025

Sergio Sesé Ballester

General Analysis of a Hybrid Rocket Model using CFD

Monografia apresentada ao Curso de Engenharia Aeronáutica, da Escola de Engenharia de São Carlos da Universidade de São Paulo, como parte dos requisitos para obtenção do título de Engenheiro Aeronáutico.

Advisor: Prof. Paulo Celso Greco Jr.

São Carlos
2025

Ficha catalográfica elaborada pela Biblioteca Prof. Dr. Sérgio Rodrigues Fontes da EESC/USP com os dados inseridos pelo(a) autor(a).

S191g

Sesé Ballester, Sergio
General Analysis of a Hybrid Rocket Model using CFD / Sergio Sesé Ballester; orientador Paulo Celso Greco Jr.. São Carlos, 2025.

Monografia (Graduação em Engenharia Aeronáutica) -- Escola de Engenharia de São Carlos da Universidade de São Paulo, 2025.

1. HRM. 2. Liquid. 3. Solid. 4. Contour Maps. 5. Flow Behavior. 6. Regression Rate. 7. Hybrid. 8. Model. I. Título.

Eduardo Graziosi Silva - CRB - 8/8907

FOLHA DE APROVAÇÃO
Approval sheet

Candidato / *Student*: Sergio Sesé Ballester

Título do TCC / *Title* : General Study of a Hybrid Rocket Model with CFD

Data de defesa / *Date*: 07/07/2025

Comissão Julgadora / *Examining committee*	**Resultado** / *result*
Professor Associado Paulo Celso Greco Júnior	APROVADO
Instituição / Affiliation: EESC - SAA	
Professor Associado Hernan Dario Ceron Muñoz	APROVADO
Instituição / Affiliation: EESC - SAA	
Professor Doutor Ricardo Afonso Angélico	Aprovado
Instituição / Affiliation: EESC - SAA	

Presidente da Banca / Chair of the Examining Committee:

Professor Associado Paulo Celso Greco Júnior
(assinatura / *signature*)

This work is dedicated to my family and friends,
whose support has been constant throughout this journey.

ACKNOWLEDGEMENTS

First of all, I would like to express my sincere gratitude to my parents Carlos Enrique Sesé and Maria Dolores Ballester. My dad who taught me the value of hard work and determination. And my mother who taught me to never give up and live every moment to the fullest. Thank you for always believing in me.

I am forever grateful to my rest of the family for their unconditional love and support throughout the journey.

Thank you to my friends from the Deus Tá Vendo house, who welcomed me into their home from the very first moment, taught me about Brazilian culture, shared unforgettable moments with me, and supported me in everything. Thank you from the bottom of my heart.

I am thankful to my home University Carlos III Madrid for giving me the knowledge to be here at this moment and the supportive research environment of the facilities. And my interchange University of São Paulo which has taught me new incredible things and made me feel at home.

To all the professors who have taught me and shown patience throughout this journey — from Spain to Brazil, thank you for giving me the privilege of sharing a classroom with you. A special mention to my advisor, Greco, who has been patient with me despite the language barrier and has taught me so much along the way.

“There has to be something very special about the boundaries of the universe.
And what could be more special than the fact that there are no boundaries?
And there should be no boundaries to human endeavor.”
Stephen Hawking

ABSTRACT

Sesé Ballester,S. **General Analysis of a Hybrid Rocket Model using CFD**. 2025. 87 p.
Monograph (Conclusion Course Paper) - Escola de Engenharia de São Carlos, Universidade de São Paulo, São Carlos, 2025.

This study investigates hybrid propellant rockets using the SARA motor from the University of Brasília and the BOITATÁ motor from the University of São Paulo, both employing nitrous oxide as a liquid oxidizer and ethylene as a solid fuel. Three models, two based on SARA geometry and one on BOITATÁ, were analyzed with the objective of achieving 1 kN of thrust and 30 bar of chamber pressure, emphasizing final thrust. Simulations were conducted using ICEM for meshing and CFD for analysis, divided into pre-processing, processing, and post-processing stages, along with MATLAB code to assess regression rates. The results compare parameters like regression rate, temperature, pressure, velocity, and mass flow rates, as well as exhaust flow characteristics, providing insights for future optimizations and potential cost reductions in upcoming university experiments.

Keywords: CFD. Hybrid Rocket Motor. ICEM. Regression Rate. Mach number. Thrust. Pressure.

RESUMO

Sesé Ballester,S. **General Analysis of a Hybrid Rocket Model using CFD**. 2025. 87 p.
Monografia (Trabalho de Conclusão de Curso) - Escola de Engenharia de São Carlos,
Universidade de São Paulo, São Carlos, 2025.

Este estudo investiga foguetes de propelente híbrido utilizando o motor SARA da Universidade de Brasília e o motor BOITATÁ da Universidade de São Paulo, ambos empregando óxido nitroso como oxidante líquido e etileno como combustível sólido. Três modelos, dois com base na geometria do SARA e um com a do BOITATÁ, foram analisados com o objetivo de alcançar 1 kN de empuxo e 30 bar de pressão na câmara de combustão, com ênfase no empuxo final. As simulações foram realizadas utilizando o ICEM para a geração de malha e o CFD para a análise, dividida nas etapas de pré-processamento, processamento e pós-processamento, além de um código em MATLAB para avaliar as taxas de regressão. Os resultados comparam parâmetros como taxa de regressão, temperatura, pressão, velocidade e vazões mássicas, assim como as características do escoamento do escapamento, oferecendo insights para otimizações futuras e potenciais reduções de custo em experimentos universitários futuros.

Palavras-chave: CFD. Motor Foguete Híbrido. ICEM. Taxa de Regressão. Número de Mach. Empuxo. Pressão.

LIST OF FIGURES

LIST OF TABLES

LIST OF ABBREVIATIONS AND ACRONYMS

HER	Hybrid Engine Rocket
SER	Solid Engine Rocket
LER	Liquid Engine Rocket
HRM	Hybrid Rocket Motor
LRM	Liquid Rocket Motor
SRM	Solid Rocket Motor
RANS	Reynolds-Averaged Navier–Stokes
CFD	Computational Fluid Dynamics
ICEM	Integrated Computational Engineering and Manufacturing
C.C.	Combustion Chamber
LPR	Liquid Propellant Rocket
SPR	Solid Propellant Rocket
HPR	Hybrid Propellant Rocket
N_2O	Nitrous oxide
C_2H_4	Ethylene
CO_2	Carbon Dioxide
N_2	Gas Nitrogen
C_2H_6	Ethane
USP	São Paulo University
LOX	Liquid Oxygen
HTPB	Hydroxyl-terminated Polybutadiene

LIST OF SYMBOLS

ρ	Density $[\frac{kg}{m^3}]$
μ	Dynamic viscosity $[\frac{kg}{ms}]$
τ	Stress tensor $[\frac{N}{m^2}]$
γ	Adiabatic coefficient $\gamma = \frac{c_p}{c_v}$
r	Regression rate $[\frac{m}{s}]$
$\dot{m}$	Mass flow rate $[\frac{kg}{s}]$
h	Enthalpy $[J]$
h_0	Stagnation Enthalpy $[J]$
h^*	Critical Enthalpy $[J]$
T	Temperature $[K]$
T_0	Stagnation Temperature $[K]$
ρ_0	Stagnation Density $[\frac{kg}{m^3}]$
a	Sound velocity $[\frac{m}{s}]$
a_0	Stagnation Sound velocity $[\frac{m}{s}]$
P	Pressure $[Pa]$
P_0	Stagnation Pressure $[Pa]$
P^*	Critical Pressure $[Pa]$
ρ^*	Critical Density $[\frac{kg}{m^3}]$
a^*	Critical Sound Velocity $[\frac{m}{s}]$
T^*	Critical Temperature $[K]$
G	Gas flow rate $[\frac{kg}{s}]$
Re	Reynolds number
M	Mach number
Q	Heat transfer $[J]$

u_x	Axial velocity $[\frac{m}{s}]$
g	Gravity $[\frac{m}{s^2}]$
T	Thrust $[N]$

CONTENTS

1 INTRODUCTION

The aerospace industry is a constantly evolving sector that plays a crucial role in the global economy and technological advancement. Space contributes significantly to daily life through system such as satellites, which provide communication and positioning services around the world and beyond. For instance, the capability to monitor Earth's climate and the observation of climate change. Moreover, space exploration offers countless possibilities for the future, including the discover of new planets and the extraction of new materials or elements that cannot be easily found on the blue planet (Learning Heroes, 2025).As such, aerospace technology is one of the greatest disruptive technologies.

The first rockets were created around 1200 AD in ancient China, as gunpowder-propelled arrows used in wars against the Mongols. During the 16th to 18th centuries, Europeans improved their efficiency and also used them in military conflicts. Between the 19th and 20th centuries, the first scientific foundations for rocketry were established by Konstantin Tsiolkovsky. Robert Goddard later became a pioneer in the construction and launch of liquid-engine rockets (LERs). During World War II, the first long-range ballistic missile was developed, the V-2 rocket. Following the war, the Space Race began, ultimately leading to the Moon landing, which was made possible by the advancements in rocket technology. Today, private companies such as SpaceX and Blue Origin are developing new technologies to propel the field forward, utilizing reusable rockets and increasing accessibility to space for commercial and private applications.

Three main types of rockets are used in the industry: liquid propellant rockets (LPR), solid propellant rockets (SPR), and hybrid propellant rockets (HPR), along with the emerging use of electric propulsion. HPRs are a mixture of LPR and SPR typically using the liquid as the oxidizer and the solid as the propellant. During the 1940s to 1960s, hybrid propellant rockets were considered the least favorable option. Nevertheless, they have been widely used in education, small-scale launches, and low-cost technology testing. Moreover, this type of rocket reached space in 2004, thanks to the company Scaled Composites.

This thesis was inspired by (Paterniti, 2024), which studies a 1 kN thrust hybrid rocket engine operating at 30 bars in the combustion chamber with two different geometries. The research is further influenced by the BOITATÁ project of 2022 (TOPUS Projetos Aeroespaciais, 2025), which is a TOPUS initiative. TOPUS is a student association passionate about rocketry, founded in 2005. The SARA motor, developed by the University of Brasilia, is also utilized; it features a different geometry compared to the TOPUS project, yet it employs the same oxidizer, nitrous oxide, and fuel, ethylene.

The high operational safety, relatively low cost, educational and experimental applicability, balance between simplicity and control, and potential for future innovation are the main reasons why hybrid rocket motors are remarkable subjects of study.

1.1 Introduction to Hybrid propulsion system

The Hybrid Rocket Motor (HRM) is a type of chemical rocket engine. As mentioned previously, this type of engine is characterized by the reaction between a fuel and an oxidizer occurring at a specific point within the motor.

There are three main types of rocket engines, which are classified according to how fuel and oxidizer are stored: liquid, solid, and hybrid rocket motors (Sutton; Biblarz, 2017). Figure 1 illustrates the typical layout of each type. In particular, Figure 1 shows the most common HRM configuration, in which the oxidizer is in liquid or gaseous form and the fuel is in solid state (Dequick; Lefebvre; Hendrick, 2021)-(Leccese; Cavallini; Pizzarelli, 2019).

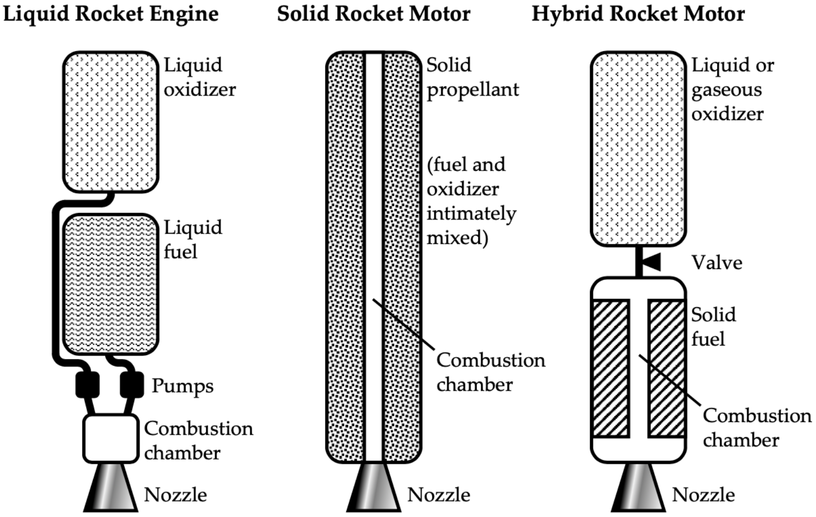

Figure 1 – Example of 3 types of chemical propulsion systems by (Dequick; Lefebvre; Hendrick, 2020).

An economical advantage is also notable, as the project and operational costs are low. The variety and exigency of the fuel quality allow for the use of more cost-effective options.

1.2 Introduction to CFD

Since the construction of a hybrid rocket requires a secure and isolated structure that can contain potential explosions in the event of HPR failure, it is essential to protect nearby personnel and infrastructure. In addition to the costs associated with equipment and rocket construction, a more reasonable option is CFD, which stands for Computational Fluid Dynamics.

CFD is a science that uses computers to predict liquid and gas flows based on the governing equations of conservation of mass, momentum, and energy (Ansys, Inc., 2024). To do so, there are three main steps that need to be followed. First (Figure 2(a)), identify the fluid flow domain to be solved. Secondly, discretize the domain into the desired mesh size and grid spacing

(Figure 2(b)). Finally, assign processors to different regions and apply the appropriate calculus equations (Figure 2(c)).

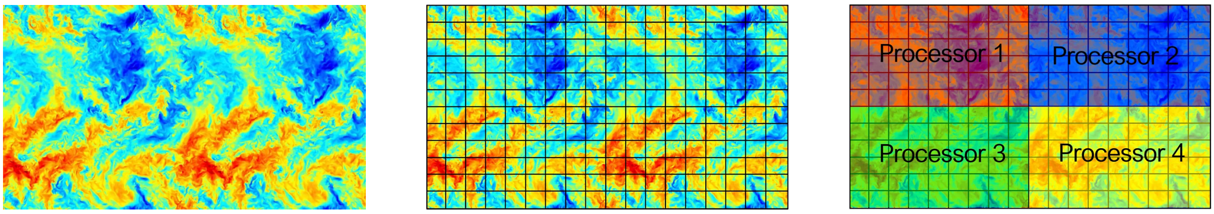

((a)) Step 1 ((b)) Step 2 ((c)) Step 3

Figure 2 – How computational fluid dynamics works by (Ansys, Inc., 2024)

Modeling fluid flow on computers is inherently difficult due to its complex nature, which involves multiphysics interactions, nonlinearity, and unsteadiness.

Multiphysics Interactions: Fluids rarely flow alone; they interact with structures (e.g., wind moving trees), other fluids (e.g., air bubbles in water), and chemical reactions (e.g., combustion in engines). Ansys CFD tools like Fluent and LS-Dyna handle these coupled problems, often by linking with structural solvers.

Nonlinearity: Fluid equations are nonlinear, which means that the fluid influences itself. Turbulence exemplifies this, as chaotic and random flow behavior is both affected by and affects heat transfer and momentum. Because of this nonlinearity, fluid dynamics problems cannot be solved analytically and require computational methods, converting calculus into algebraic problems.

Unsteadiness: Turbulent flows are inherently unsteady, with flow properties changing over time at fixed points. Capturing this behavior requires time-resolved simulations, which are computationally expensive.

Turbulence remains one of the greatest challenges in classical physics, famously described by Richard Feynman as “the most important unsolved problem.” Although CFD does not mathematically solve turbulence, it enables engineers to model its effects for practical design purposes.

There are limitations when using CFD regarding flow conditions, such as in the case of highly rarefied gases, which are characteristic of the stratosphere. By default, the software solves the equations in the Reynolds-Averaged Navier–Stokes (RANS) form, which is widely used in the industry.

This approach has the advantage of a computational cost that makes it feasible to simulate high-Reynolds-number flows over complex geometries. However, it has the drawback of requiring the use of so-called turbulence models. These models are necessary to account for the effects of turbulence, as the RANS formulation filters out (removes) the high-frequency random fluctuations that are typical of turbulent flow conditions.

1.3 Objective

The thesis referenced in (Paterniti, 2024) focuses on fuel injection, whereas this thesis emphasizes the overall performance of the rocket. The model is studied using the software *ANSYS CFD*, which employs nitrous oxide (N_2O) as the oxidizer and ethylene (C_2H_4) as the fuel. Advanced equations governing fluid dynamics and heat transfer are utilized to achieve an accurate resolution of the phenomena associated with hybrid propellant rockets. The fuel mixture plays a critical role in the rocket's performance. This analysis includes:

- The evolution of pressure, temperature, and velocity in the combustion chamber and exhaust.
- The behavior of the reactive flows and their products.
- Study of the regression rate of the model.

This computational approach enables comparisons between different configurations and operational parameters without the use of a real experiment, providing a comprehensive understanding of the behavior of hybrid motors. Additionally, it offers opportunities for future adjustments and optimizations.

This thesis is carried out to support the students of the USP in developing a hybrid rocket. The following simulations aim to assist in the early decision-making stages for the physical, non-computational implementation of this experiment.

1.4 State of art

During the last few years, the space sector has been improved by new companies, including those that have made space accessible for tourism. This type of mission has been carried out by Blue Origin, a company founded by Jeff Bezos. It is a private aerospace company that has been developing technologies for space exploration and space tourism.

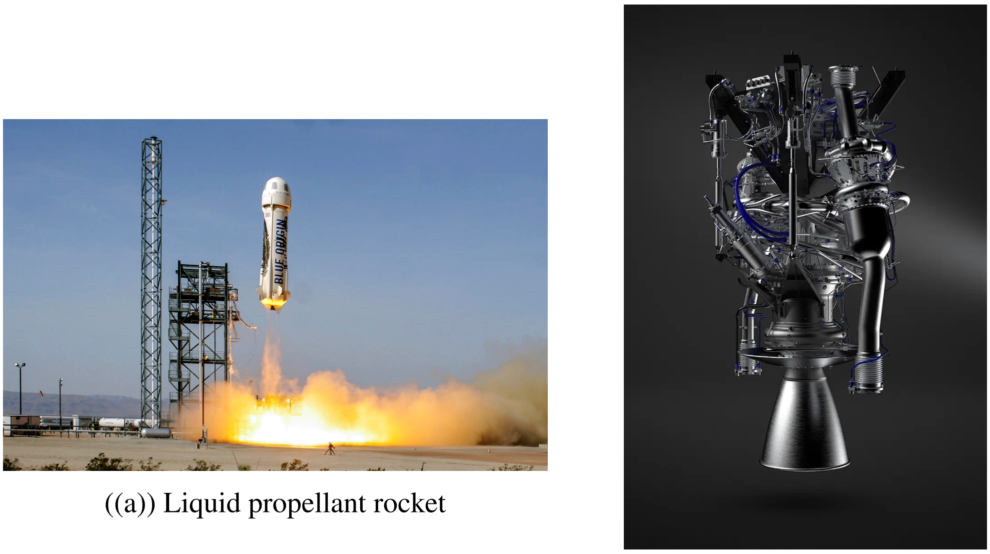

((a)) Liquid propellant rocket

((b)) BE-3PM rocket engine(2015)

Figure 3 – Blue Origin equipment by (Blue Origin, 2025).

In the near future, hybrid propellant rockets could become a better option for this type of mission. As explained by (Sutton; Biblarz, 2017), they offer several advantages over liquid propellant rockets, such as the ability to stop and restart the rocket at will, and they are safer and simpler than bipropellant liquid rockets. Furthermore, emphasizing their advantages, according to (Conde; Mora, 2025), HPRs can be controlled during flight by regulating the oxidizer flux. This control allows for difficult maneuvers, from changing to enabling a controlled landing. Additionally, the hybrid rockets are safer than the solid ones because, in case of emergency, they can switch off. Since they keep the oxidant and the propellant in different sections, the probability of auto-ignition or self-explosion is reduced. This risk is significantly higher with solid propellants. In terms of cost, hybrid rockets are cheaper than liquids ones, however, hybrids rockets are more expensive than solids rockets.

One of the most common oxidizers is liquid oxygen (LOX), but as the article (Kopacz *et al.*, 2022) explains, hydrogen peroxide (H_2O_2) is a better alternative than LOX, as it is safer and more efficient. In this case, nitrous oxide (N_2O) will be used, which is also a safer oxidizer than LOX, as confirmed in (Handling…, Desconocido). With the use of the same oxidizer, there are real sub-orbital missions of HPR carried out by the company Virgin Galactic for the tourist sector. The engine used is called RocketMotor2 (RM2), which can produce approximately 310 kN of thrust, with a specific impulse of 250 seconds. This information is provided by the article (Schmidle,).

Figure 4 – Hybrid Rocket VSS Unity by (Virgin Galactic, 2025).

They are not the only companies working with hybrid rockets. Companies such as Sierra Nevada Corporation (Sierra Nevada Corporation, 2013a)–(Sierra Nevada Corporation, 2013b)–(Sierra Nevada Corporation, 2020) are also involved. SNC is a private company in the aerospace, defense, and advanced technology sectors. It works with the U.S. government as well as commercial clients. They have collaborated with Virgin Galactic on the development of the rocket SpaceShipTwo (SS2), as mentioned earlier. Furthermore, they have patented the VORTEX motor, which is a hybrid propulsion system. This motor is part of the Operational Fires (OpFires) program under the Defense Advanced Research Projects Agency. The latest tests of VORTEX have demonstrated positive results, showing its capability to store energy in a reduced volume, with deep regulation capability and smooth start-stop operation on demand.

A European company known as Nammo has developed a hybrid propellant rocket called Nucleus 5, which was launched in 2018 in Norway. Nucleus was the first sounding rocket of Norway. The company emphasizes the advantages of HPRs, such as start-stop capability, which enables accurate control of the 30 kN of thrust and allows for different flight patterns, such as horizontal flight (Nammo, 2023).

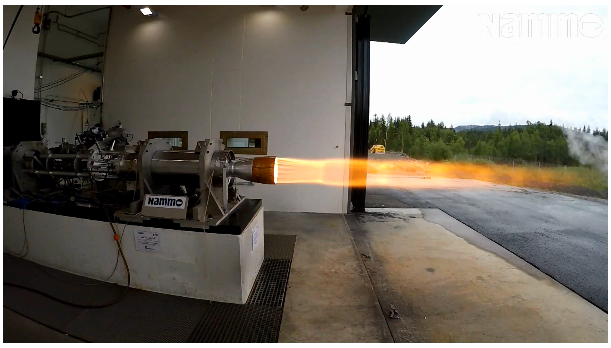

Figure 5 – Hybrid Rocket Nucleus test before launch by (Nammo, 2023)

The HYPR Space Technologies company (HYPR Space Technologies, 2025) is focused on the development of systems for hybrid rocket propulsion, with the mission to provide safer, more efficient, and accessible launch solutions. Their technology combines non-toxic solid fuel with a liquid oxidizer, offering hybrid motors that reduce costs, improve safety, and facilitate flight control compared to other traditional motors. The company is committed to innovation in the sector as a versatile and trusted alternative for the future of aerospace transportation. Their missions include both sub-orbital and orbital flights.

According to the article (Kopacz *et al.*, 2022), research is focused on finding a new fuel that never stops, improving combustion efficiency, and offering the best thrust possible. For example, polyethylene is proposed as an alternative. Moreover, polyethylene is not the only material that improves combustion efficiency; PTFE (polytetrafluoroethylene) is another option. As mentioned by Marothiya and Periyapatna (2022) (capítulo, 2022), introducing mechanically activated aluminum into the propellant mixture enhances the combustion rate and reduces the problem of aluminum agglomeration. For small experiments like this one, paraffin is used because it has reliable combustion properties, is easy to handle, and is economical. Other advantages include being less toxic and less reactive than other solid fuels.

1.4.1 Advantages and Disadvantages

The selection of the configuration for a mission is a key parameter for its success. This choice must involve careful consideration of the circumstances or incidents that the rocket may encounter during operation. It is essential to evaluate the advantages and disadvantages of hybrid propellant rockets (HPR) (Corteguera, 2013)-(Sutton; Biblarz, 2017).

Firstly, the primary advantage of this rocket compared to others is safety. The fuel is inert; in other words, it does not undergo any chemical reaction under normal ambient pressure and temperature conditions. Consequently, the fuel will not ignite accidentally due to electrostatic discharge, vibrations during manufacturing, assembly, transportation, or operation. The system is not explosive; as illustrated in Figure 1, the fuel and oxidizer are stored in separate compartments.

Furthermore, the fuel is the last component to be assembled. In the event of an accident, the engine can be shut down by cutting off the flow of the oxidizer.

In addition to safety, this type of rocket has potential applications in warfare, as hybrid rocket motors (HRMs) are resistant to bullet impacts, fires beneath the vehicle, and explosions from nearby munitions or other rockets.

Considering the information mentioned above and the significant amount of space debris orbiting the planet, hybrid rockets are a strong candidate for space missions, regardless of the risk of collisions with such debris.

This type of motor is easily adjustable in different parameters:

The motor is easily regulated thanks to a valve that controls the quantity of oxidizer mass flux entering the combustion chamber. The interaction between the oxidizer and fuel produces hypergolic ignition, meaning that combustion occurs upon contact between the two without the need for an igniter.

Similar to the behavior of liquid propellant rockets (LPRs), hybrid rocket motors exhibit low sensitivity to ambient pressure. Variations in ambient temperature between tests have an insignificant effect on the pressure in the combustion chamber due to the minimal evaporation ratio of the fuel in response to temperature changes.

Another advantage is the variety of options available for selecting the combustion mixture. In this simulation, nitrous oxide will be used with ethylene; however, there are other types of combustion mixtures. One of the most well-known combinations is liquid oxygen (LOX) with hydroxyl-terminated polybutadiene (HTPB).

However, there are disadvantages that hinder the full development of these systems on a larger scale.

Firstly, the slow evaporation velocity of the fuel is not suitable for operational conditions. This results in variations in the O/F ratio (oxidizer mass to fuel mass) throughout the stationary regime of operation, which does not produce a constant thrust.

Secondly, the low volumetric density of the fuel presents a challenge. As a consequence of the low evaporation velocity, it is necessary to have a large grain surface area of fuel to achieve the required thrust.

In addition, this type of motor exhibits low grain combustion efficiency and a lower specific impulse compared to other motors. Unlike liquid propellant rockets (LPRs) or solid propellant rockets (SPRs), this motor operates with a diffusion flame rather than a premixed flame.

The transitory period of ignition is slower, as is the response to the regulated flow from the fuel supplier. However, this is not significant in practice.

1.4.2 Regression Rate

In this type of configuration, since the fuel grain does not contain oxidizer, combustion occurs only in the gas state. Knowing this, fuel surface regression is closely linked to fluid dynamics in the combustion port and heat transfer to the fuel grain surface. In the boundary layer, the primary region is contained within a narrow flame zone that develops and grows on the fuel grain surface. Heat is transferred to the fuel grain surface through convection and radiation. Since hybrid studies are mostly empirical, it is well understood that motor characteristics depend strongly on the propellant system, as well as the scale and configuration of the combustion chamber.

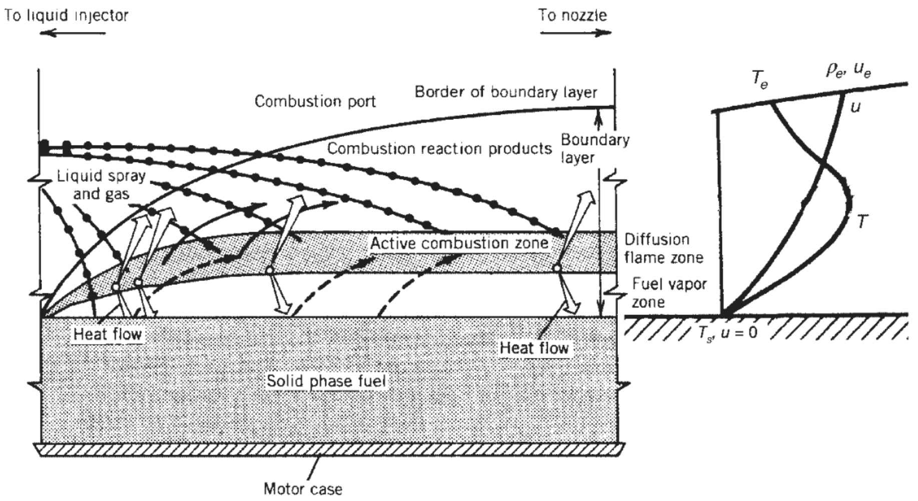

Figure 6 – Simplified model of a diffusion-controlled hybrid combustion process by (Sutton; Biblarz, 2017).

Figure 6 presents a simplified model of the hybrid combustion process for a non-metallized (or low radiation) fuel system. The fuel vaporized by flame zone heating flows away from the surface toward the flame region, while the oxidizer is convected from the core flow to the flame zone via turbulent diffusion. The flame establishes itself within the boundary layer according to the combustion stoichiometry. The thickness of the flame zone is primarily determined by the rate of oxidation reactions, which depend on local pressures and typically follow an exponential temperature dependence.

In the Hybrid Rocket Motor (HRM), regression refers to the rate of consumption of the solid fuel within the motor during the combustion process. Specifically, it denotes the rate at which the surface of the solid grain burns and diminishes in size, thereby allowing it to react with the oxidizer. This rate is critical, as it determines the quantity of fuel consumed per unit of time and directly influences both the thrust and burn duration of the motor. The regression rate is contingent upon several factors, including the oxidizer flow rate, grain geometry, temperature, and the characteristics of the boundary layer present on the fuel surface.

The development of the boundary layer in the grain, which affects the regression rate, depends not only on pressure and temperature but also on the composition of the grain, the maximum flux of the oxidizer, and the dimensions of the combustion port. As illustrated in Figure 7, there are three regimes that depend on the maximum flux of the oxidizer. At low flow rates, radiative heat transfer affects the optical transmissivity of the gas, potentially causing the fuel grain to melt or decompose. In the intermediate range, heat and mass transfer are turbulent, and the regression rate exhibits an approximate dependence on $G^{0.8}$. At high flow rates, gas-phase chemical kinetics influence combustion, and a “flooding limit” may occur, wherein the flame is extinguished due to excess oxidizer. This phenomenon is influenced by pressure and chemical reactions, as noted by (Sutton; Biblarz, 2017)- (Rampazzo; Barato, 2023)-(Faenza *et al.*, 2015).

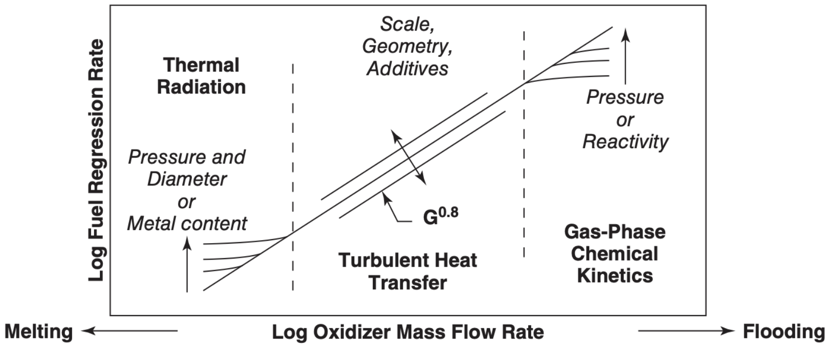

Figure 7 – Hybrid regimes of regression rate dependencies by (Sutton; Biblarz, 2017)

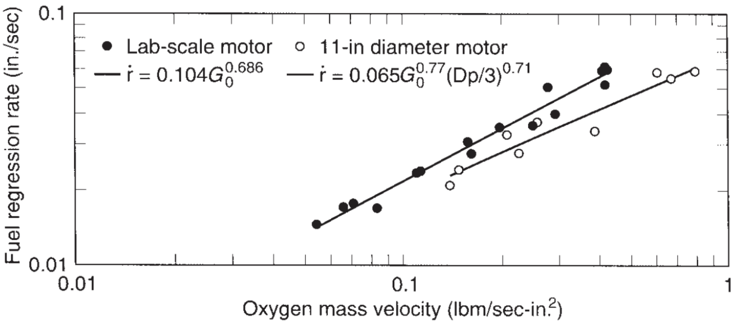

Figure 8 – Curve of the regression rate by (Sutton; Biblarz, 2017)

Three behaviors can be distinguished according to the oxidizer flux 1.1 over the surface. The region in the middle of the figure 7, intermediate range, can be modeled as 1.2.

$$G_0 = \rho_0 u_0 = \frac{\dot{m}}{A_t} \quad [\frac{kg}{m^2 s}] \ \ or \ \ [\frac{lbm}{in^2 s}] \tag{1.1}$$

$$\dot{r} = aG_0^n \quad [\frac{mm}{s}] \ \ or \ \ [\frac{in}{s}] \tag{1.2}$$

Where $\dot{r}$ represents the regression rate, a is the regression rate constant, which has its own units, and n is the exponent. The fuel regression rate of a hybrid rocket is approximately one-third that of a typical solid rocket. This rate is coupled with the fuel of the oxidizer (G) that enters the combustion chamber; in other words, modifying this rate proves challenging. Furthermore, this regression is smaller for larger motor scales that operate at the same oxidizer flux. In the figure 8 it can be seen the previous affirmation as higher the scale less will be the rate;

- Small rockets: $\dot{r} = 0.104\mathring{u}G^{0.686}$
- 11-in diameter: $\dot{r} = 0.065\mathring{u}G^{0.77}(\frac{D_p}{3})^{0.71}$

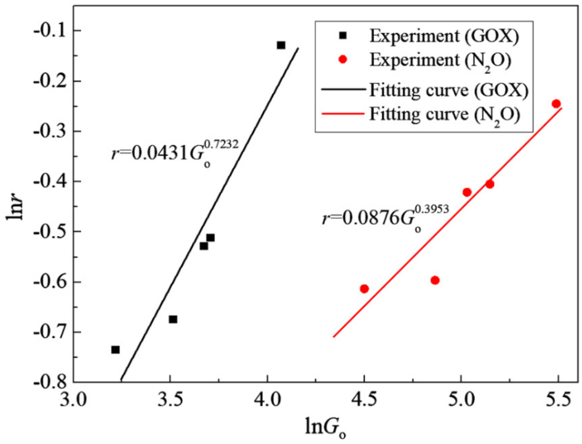

Figure 9 – Curve of regression rate by (Liu *et al.*, 2020)

It shows a larger dependence on the diameter of the port combustion, D_p. Other more complex laws include; x axial position, μ viscosity of combustion gas, β dimensionless fuel flux, ρ_f fuel density, p pressure, D_p port diameter

- $\dot{r} = 0.036\frac{G^{0.8}}{\rho_f}(\frac{D_p}{3})^{0.71}$
- $\dot{r} = aG^n p_1^m D_p^l$

To be more precise, the experiment (Liu *et al.*, 2020) has used the same oxidizer as in this simulation N_2O. It is possible to use the same approximation for a and n using their example for this simulation. In figure 9, the black curve and the points represent the experiment for GOX, gaseous oxygen, which has a strong oxidation capability. And the red curve, as in this simulation, is associated to the oxidizer N_2O which is going to be used in the final results as an approximation.

$$r = 0.0876G_o^{0.3953} \tag{1.3}$$

Combustion inefficiency is one of the primary challenges faced by hybrid rockets, particularly if the mixture between fuel and oxidizer is insufficiently optimized. Furthermore, increasing turbulence and meticulously designing the geometry of the grain can lead to improvements in combustion efficiency. Additionally, to reduce fuel slivers, the design of the grain plays a fundamental role.

1.4.3 Thrust

The simple answer to why rockets can fly is thrust, which is explained by Newton's third law. Thrust is the force produced by the rocket propulsion system, acting at the vehicle's center of mass (Sutton; Biblarz, 2017). The rocket experiences this force through the ejection of propellant at high velocities. This force can be calculated using the momentum equation. Momentum is a vector quantity defined as the product of mass and its vector velocity. The idealized thrust can be expressed as shown in equation 1.6; however, this force is only valid when the pressure in the combustion chamber equals the ambient pressure.

$$F = \frac{d(mv_2)}{dt} = \dot{m}v_2 \tag{1.4}$$

Figure 10 illustrates the pressure distribution along the rocket, demonstrating that the pressure inside the combustion chamber is fundamental to the final thrust. The greater the pressure inside the chamber compared to the ambient pressure, the larger the resultant thrust.

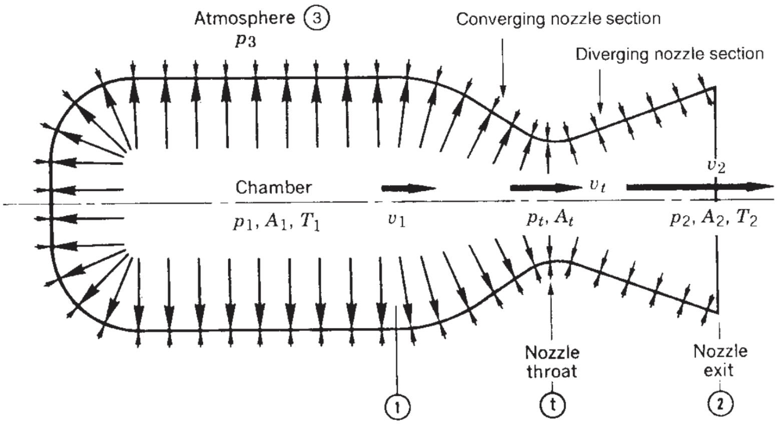

Figure 10 – Gas pressure distribution along the rocket by (Sutton; Biblarz, 2017)

Due to changes in altitude, ambient pressure can vary significantly, which in turn affects thrust. The thrust also changes in response to the imbalances produced by pressures p_2 and p_3 in the exit area.

$$F = \dot{m}v_2 + (p_2 - p_3)A_2 \tag{1.5}$$

When the rocket is in vacuum space $p3 = 0$ and the pressure thrust becomes a maximum.

$$F = \dot{m}v_2 + p_2 A_2 \tag{1.6}$$

1.4.4 Impulse

Impulse is defined as the thrust integrated over a given period of time; in other words, it is the thrust (F) multiplied by the duration (t) , (Sutton; Biblarz, 2017).

$$I_t = \int_0^t F dt = Ft \tag{1.7}$$

This total impulse is proportional to the total energy released by or into all of the propellant utilized by the propulsion system.

This total impulse is proportional to the total energy released by or absorbed by all of the propellant utilized by the propulsion system.

$$I_s = \frac{\int_0^t F dt}{g_0 \int_0^t \dot{m} dt} = \frac{I_t}{g_0 m_p} \tag{1.8}$$

Equation 1.8 is applicable to any rocket propulsion system and provides a time-averaged impulse value expressed in seconds.

1.4.5 Effective exhaust velocity

At the exit of the nozzle, the velocity is not uniform across the area, making accurate measurement challenging. To approximate this value, a uniform axial velocity is assumed, which employs one-dimensional problem descriptions. The effective exhaust velocity is defined as:

$$c = I_s g_0 = \frac{F}{\dot{m}} \tag{1.9}$$

1.4.6 Ideal flows

When fluid motion occurs at large Reynolds numbers, viscous stresses and thermal heat conduction become negligible in most of the flow field. Under these conditions, the Navier-Stokes equations reduce to the so-called Euler equations, which can be further simplified under conditions of practical interest (Sutton; Biblarz, 2017). This simplification is essential for understanding concepts such as the Mach number, shock waves, Prandtl-Meyer expansion, and stagnation conditions.

$$Re = \frac{\rho v S}{\mu} \tag{1.10}$$

$$Re = \frac{\rho U L}{\mu} \tag{1.11}$$

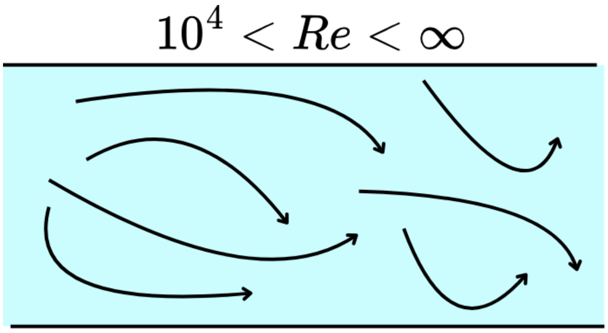

Figure 11 – Turbulent flow

The equation 1.11 represents the Reynolds number (Re) inside a pipe. Depending on the value of the Reynolds number, it is possible to determine how the fluid is moving within the pipe. If the value is $0 < Re < 10^3$, the fluid will be considered laminar 12, characterized by smooth and steady flow. If the Reynolds number falls between $10^4 < Re < \infty$, the flow will be classified as turbulent 11, during which its behavior begins to fluctuate and becomes agitated.

There exists a transitional regime between these two behaviors when $10^3 < Re < 10^4$.(White, 2011).

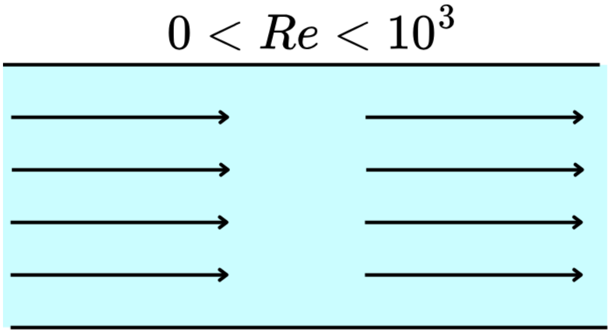

Figure 12 – Laminar flow

1.4.6.1 Sound velocity

Another thermodynamic law has to be defined beside the enthalpy and entropy, it is the sound velocity, which is the velocity at which the small pressure perturbations propagate in a compressible medium at rest. For a perfect liquid of constant ρ, the velocity of sound is infinite. But for a perfect gas is a function of temperature. Where γ is the relation between constant pressure and constant volume $\gamma = \frac{c_p}{c_v}$

$$a = (\frac{\gamma P}{\rho})^{1/2} = (\gamma R_g T)^{1/2} \tag{1.12}$$

1.4.6.2 Mach Number

The Mach number is defined as the ratio between the velocity of the system, denoted as v, and the sound velocity, denoted as a. The flow can be categorized based on the value of the Mach number: it is considered subsonic if $M < 1$, sonic if $M = 1$, and supersonic if $M > 1$.

$$M = \frac{v}{a} \tag{1.13}$$

1.4.6.3 Stagnation Conditions

The stagnation condition occurs when the fluid suddenly stops, resulting in a velocity of zero. By utilizing the Mach number, it is possible to calculate the stagnation conditions.

$$T_0 = T(1 + \frac{\gamma - 1}{2} M^2) \tag{1.14}$$

$$P_0 = P(1 + \frac{\gamma - 1}{2} M^2)^{(\frac{\gamma+1}{2})} \tag{1.15}$$

$$a_0 = a(1 + \frac{\gamma - 1}{2} M^2)^{\frac{1}{2}} \tag{1.16}$$

$$\rho_0 = \rho(1 + \frac{\gamma - 1}{2} M^2)^{\frac{1}{\gamma-1}} \tag{1.17}$$

1.4.6.4 Flow at the chamber exit

The critical values where the flow is sonic can be determined as functions of M for steady gas flow in pipes.

$$\frac{h_0}{h^*} = \frac{T_0}{T^*} = (\frac{a_0}{a^*})^2 = (\frac{P_0}{P^*})^{\frac{(\gamma-1)}{\gamma}} = (\frac{\rho_0}{\rho^*})^{(\gamma-1)} = \frac{\gamma+1}{2} \tag{1.18}$$

The gas flow rate of the critical section can also be calculated:

$$G = G^* = \rho_0 a_0 A^* (\frac{\gamma+1}{2})^{-\frac{\gamma+1}{2(\gamma-1)}} \tag{1.19}$$

Now, considering that p_a is the atmospheric pressure and introducing the subscript c to refer to the container, we have $p_c = p_0$, $a_c = a_0$, $T_c = T_0$, and $\rho_c = \rho_0$. Furthermore, a relationship is established between p_0 and p_a, leading to two distinct situations: In Table 1, the flow behavior is illustrated in relation to differences in pressure. A choked flow occurs when the fluid at the throat has a Mach number of $M = 1$. In this condition, the mass flow rate that is passing through the throat does not increase; in other words, it is limited.

Condition	**Formulas**	**Fluxes**
$\frac{p_0}{p_a} < \left(\frac{\gamma+1}{2}\right)^{\frac{\gamma}{\gamma-1}}$	$M = \left(\frac{2}{\gamma-1}\right)^{1/2} \left[(\frac{p_c}{p_a})^{(\gamma-1)/\gamma} - 1 \right]^{1/2}$ $G = \rho_c a_c A \left(\frac{2}{\gamma-1}\right)^{1/2} \left(\frac{p_c}{p_a}\right)^{(\gamma+1)/(2\gamma)} \left[(\frac{p_c}{p_a})^{(\gamma-1)/\gamma} - 1 \right]^{1/2}$	Non Choked
$\frac{p_0}{p_a} \geq \left(\frac{\gamma+1}{2}\right)^{\frac{\gamma}{\gamma-1}}$	$M = 1$ $G = G^* = \rho_0 a_0 A^* \left(\frac{\gamma+1}{2}\right)^{-\frac{\gamma+1}{2(\gamma-1)}}$	Choked

Table 1 – Situation for choked and non-choked flow

1.4.7 Shock Wave

Shock waves are nonlinear waves that propagate at supersonic speeds and cause abrupt and instantaneous changes in the properties of the medium, such as pressure, temperature, density, and velocity as the fluid is compressed. These waves are generated when a disturbance travels faster than the local speed of sound, as occurs in supersonic flights or explosions (Gopalan, 2008).

1.4.7.1 Characteristics

Shock waves are very thin wave fronts where abrupt changes in thermodynamic variables occur. They differ from ordinary sound waves, which have small amplitudes and cause reversible changes. Shock waves form in media that allow for propagation (they do not occur in a vacuum). They can be classified as “strong” or “weak,” depending on the magnitude of the change in the medium. Furthermore, there are normal shock waves that are perpendicular to the flow, and oblique shock waves that are produced at a concave corner.

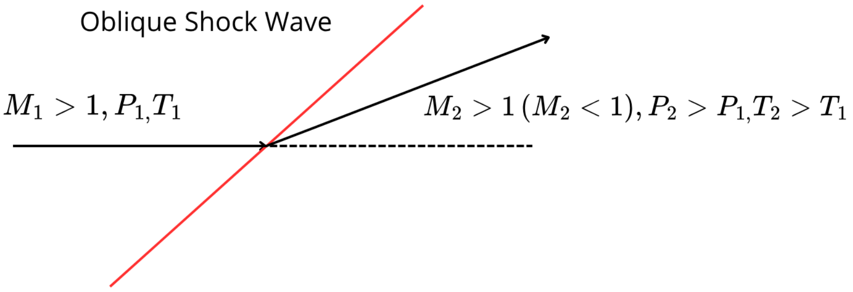

Figure 13 – Example of a shock wave

There are several differences between normal and oblique shock waves, the most significant being that the Mach number behind a normal shock is subsonic, while in oblique shock waves, it can be either subsonic or supersonic and may change direction. The similarities include an increase in entropy, as the process is not isentropic; an increase in temperature behind the shock wave; an increase in pressure; and a decrease in the Mach number (Sánchez; Rodriguez, 2021)-(Gopalan, 2008).

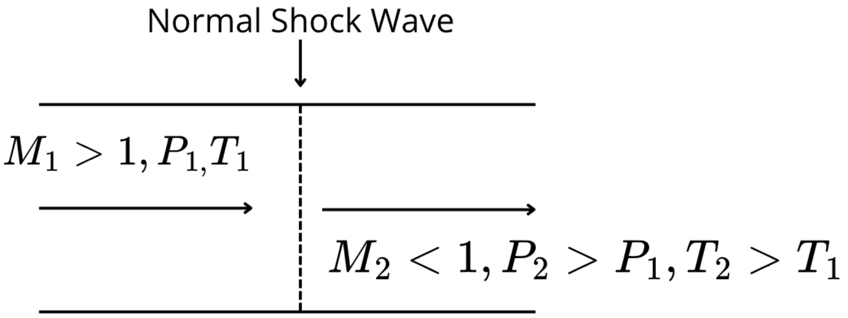

Figure 14 – Example of a normal shock wave

1.4.7.2 Prandtl-Meyer expansion

The Prandtl-Meyer expansion occurs when the flow is supersonic (Sánchez; Rodriguez, 2021), with $M > 1$. When the stream passes through a convex corner, the flow undergoes smooth isentropic expansion, and Mach waves are created as the direction of the stream changes. These Mach waves cannot be altered using shock waves because they represent an expansion rather than compression. Behind the expansion, the pressure decreases $(p_1 > p_2)$, the Mach number increases $(M_1 > M_2)$, and both temperature and density also decrease.

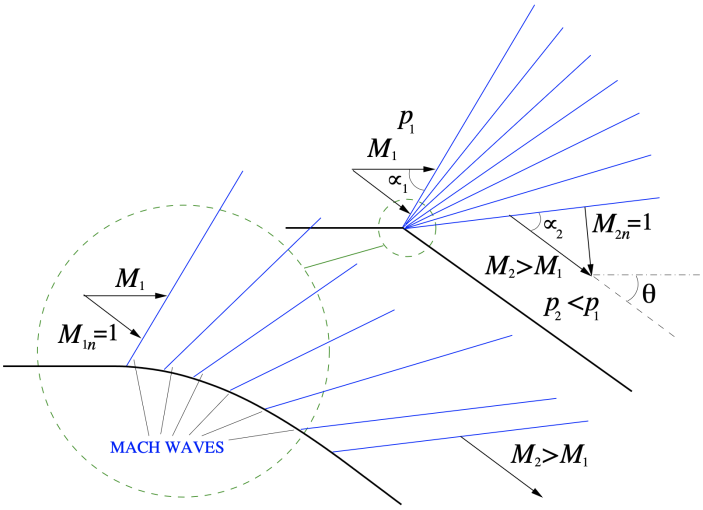

Figure 15 – Example of a Prandtl-Meyer expansion (Sánchez; Rodriguez, 2021)

1.4.7.3 Convergent divergent nozzle

In a rocket, the exit is typically a convergent-divergent nozzle. The geometry of the nozzle is defined by the exit area A_e and the throat area A_t. The nozzle is connected to a reservoir with pressure P_0 and discharges to the atmosphere, where the pressure is P_a. As illustrated in Figure 16, different results emerge depending on the value of $\frac{P_a}{P_0}$ (Sánchez; Rodriguez, 2021). The supersonic case f demonstrates how the subsonic flow enters through the throat, becomes sonic, and discharges as supersonic into the ambient atmosphere through the divergent section, leaving the nozzle with $p_e = p_a$. Consequently, neither expansions nor compressions are needed to adapt the pressure to the ambient value.

The flow is considered overexpanded when the pressure at the exit is lower than the ambient pressure. This condition creates two shock waves that converge along the centerline, resulting in the formation of an additional two shock waves, ultimately leading to a Prandtl-Meyer expansion that reduces the pressure but increases the Mach number. In Figure 16, the situation described corresponds to case e in the figure.

The flow is called underexpanded when the pressure at the outlet of the nozzle is higher than the ambient one, $p_e > p_a$. This condition creates a Prandtl-Meyer expansion, which accelerates the fluid and decreases the pressure until it reaches the ambient pressure. In Figure 16, the underexpanded flow is associated with case g. In addition, there are different types of underexpanded structures, such as; moderate, high and extreme, depending on the value of the pressure ratio $\frac{p_e}{p_a}$ (Mehta *et al.*, 2011; Guardone; Parsani; Vigevano, 2007; Manning; Penley, 1963; Franquet *et al.*, 2015).

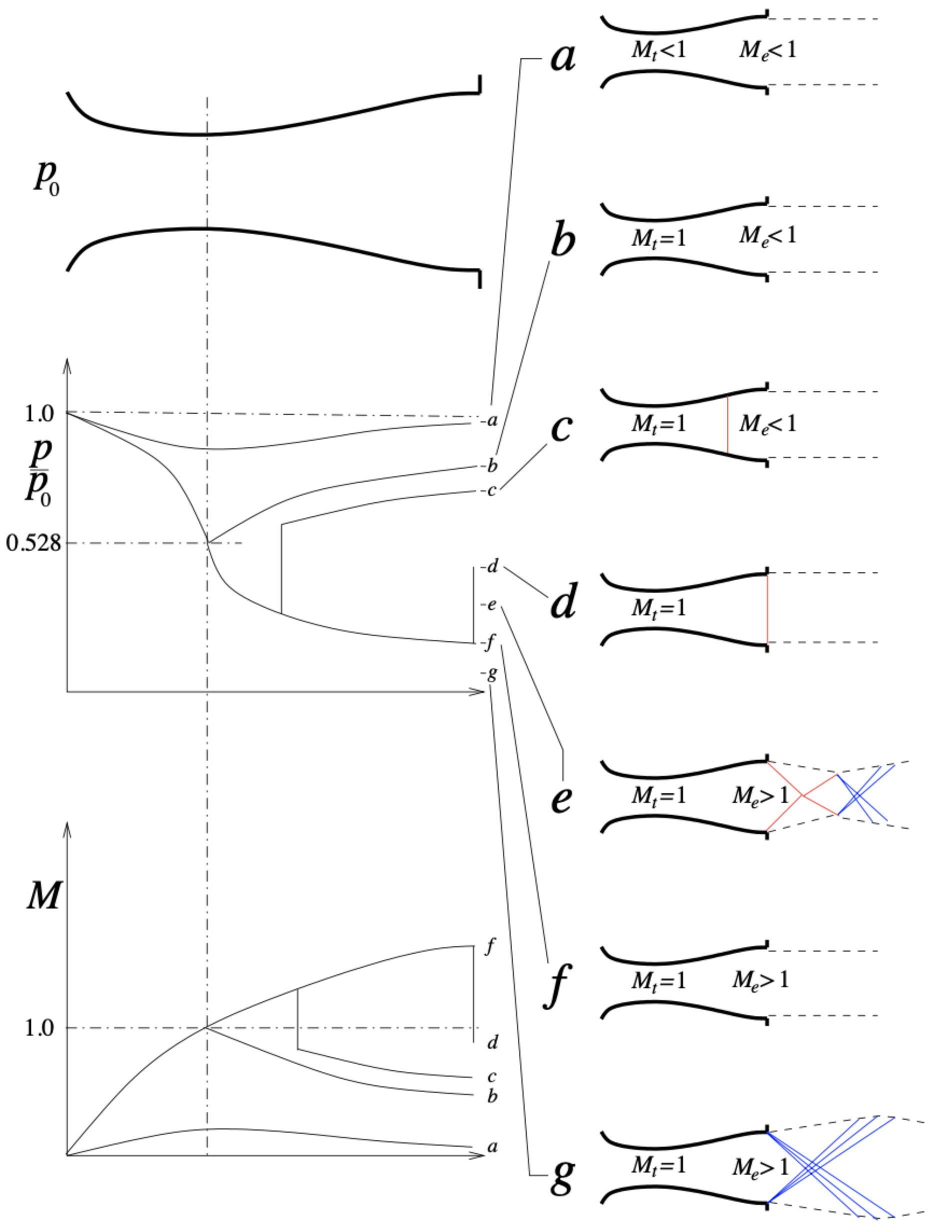

Figure 16 – Flow in a convergent-divergent nozzle (Sánchez; Rodriguez, 2021)

1.4.8 Boundary Layer

The boundary layer is the thin region that forms in the fluid when it flows over a surface (White, 2011). The velocity changes from zero at the surface to nearly the free-stream velocity far away from the surface due to the fluid's viscosity. It can be either smooth (laminar) or chaotic (turbulent). This layer is significant because it influences resistance, heat transfer, and the behavior of drag in various systems.

1.4.9 No Slip Condition

The no-slip condition is an important principle in fluid mechanics. This condition states that, whether liquid or gas, the velocity of a fluid at a solid boundary is zero (Savvides, 2023).

A force causes the fluid to slow down and eventually stop when it comes into contact with a solid surface. This force may result from van der Waals forces, electrostatic forces, and chemical interactions between the fluid and the solid surface.

2 GOVERNING EQUATIONS

As was introduced before, CFD are used different equations but principally it is with the Reynolds-Averaged Navier-Stokes for modelladed turbulent fluxes. This equations are extracted from (ANSYS Inc., 2021). Approximate solutions for the overall properties of a fluid system can be obtained by applying the integral forms of the conservation equations for mass, momentum, and energy over a chosen control volume. This approach generally requires simplifying assumptions, such as uniform spatial distributions and neglecting terms with relatively small contributions to the overall balances.

However, the integral approach is not suitable for calculating local flow properties, such as point-wise distributions of velocity, density, or pressure. To analyze local behavior, the integral conservation equations must be transformed using Gauss's theorem to express the local rate balances.

The transformation of integral conservation equations into partial differential equations allows for the analysis of local flow properties. This set of equations, essential for understanding fluid dynamics, must be resolved with specific initial and boundary conditions to accurately predict flow behavior. The most significant equations in this context include the Continuity Equation, which ensures mass conservation, the Momentum Equation, which governs motion, and the Energy Equation, which relates to thermal dynamics. While additional equations exist within computational fluid dynamics (CFD), these are the foundational equations critical for the thesis at hand.

2.1 The Continuity and Momentum Equations

The Continuity Equation:

$$\frac{\partial \rho}{\partial t} + \nabla \cdot (\rho \vec{v}) = S_m \tag{2.1}$$

The equation 2.1 is the general form of the mass conservation equation and is valid for incompressible as well as compressible flows where ρ is the density, $\vec{v}$ is the velocity and S_m is the mass added to the continuous phase from the dispersed second phase (for example, due to vaporization of liquid droplets) and any user-defined sources.

The Momentum Equations:

$$\frac{\partial}{\partial t}(\rho \vec{v}) + \nabla \cdot (\rho \vec{v}\vec{v}) = -\nabla p + \nabla \cdot \bar{\bar{\tau}} + \rho \vec{g} + \vec{F} \tag{2.2}$$

The momentum equation is described in an inertial (non-acceleration) reference frame where p is the static pressure, $\bar{\bar{\tau}}$ is the stress tensor, and $\rho \vec{g}$ and $\vec{F}$ are the gravitational body force and external body forces.

Where the stress tensor τ is related to the strain rate by:

$$\bar{\bar{\tau}} = \mu \left[\left(\nabla \vec{v} + \nabla \vec{v}^{T} \right) - \frac{2}{3} \left(\nabla \cdot \vec{v} \right) I \right] \tag{2.3}$$

In the equation 2.3 μ is the molecular viscosity, I is the unit tensor, and on the right hand side is the effect of volume dilation.

2.2 The Energy Equation

The Total Energy Equation is the equation 2.4, according to the first thermodynamic law, the total energy contained contained in a fluid volume may change due to heat addition through the bounding fluid surface or by the chemical reaction or radiation inside the fluid volume. The Navier Stoke Energy equation is the following:

$$\frac{\partial(\rho h_{\text{tot}})}{\partial t} + \frac{\partial p}{\partial t} + \nabla \cdot (\rho U h_{\text{tot}}) = \nabla \cdot (\lambda \nabla T) + \nabla \cdot (U \cdot \tau) + U \cdot S_M + S_E \tag{2.4}$$

In this equation, ρ is the fluid density, and h_{tot} is the total enthalpy, defined as $h_{\text{tot}} = h + \frac{1}{2}U^2$, where h is the static enthalpy and U is the magnitude of the velocity vector. The term $\frac{\partial(\rho h_{\text{tot}})}{\partial t}$ represents the local (unsteady) change in energy per unit volume, while $\frac{\partial p}{\partial t}$ accounts for the compressibility work. The convective transport of energy is given by $\nabla \cdot (\rho \vec{U} h_{\text{tot}})$. Heat conduction is described by $\nabla \cdot (\lambda \nabla T)$, where λ is the thermal conductivity. The term $\nabla \cdot (\vec{U} \cdot \bar{\tau})$ represents the work done by viscous stresses, with $\bar{\tau}$ being the viscous stress tensor. The product $\vec{U} \cdot S_M$ accounts for work done by momentum sources such as fans or propellers, and S_E represents external energy sources like chemical reactions or radiative heat transfer.

Where the total enthalpy h_{tot} is related to the static enthalpy $h(T, p)$ by:

$$h_{\text{tot}} = h + \frac{1}{2}U^2 \tag{2.5}$$

In this expression, the term $\frac{1}{2}U^2$ corresponds to the kinetic energy per unit mass, where U is the magnitude of the velocity vector of the fluid. Thus, h_{tot} accounts for both the thermal and mechanical (kinetic) contributions to the total energy content of a fluid particle.

2.3 Reynolds-Average Navier-Stokes

Turbulence modeling involves developing simplified partial differential equations to predict turbulent flows by making suitable approximations of the Navier Equations by (Alfonsi, 2009). In the point of view of the Navier-Stokes equations given by the RANS, they decompose the variables in variables of flux in mean and fluctuating parts. As inserting this decomposition in the Navier Stokes and later average the equations, it appears the Reynolds-stress tensor, it is an unknown term that must be modeled to solve the RANS by (Alfonsi, 2009).

Reynolds Decomposition and Averaging

The flow of a viscous incompressible fluid constant properties is governed by the Navier-Stokes:

$$\frac{\partial u_i}{\partial t}+\frac{\partial}{\partial x_j}(u_i u_j)=-\frac{\partial p}{\partial x_i}+\nu\frac{\partial^2 u_i}{\partial x_j \partial x_j} \tag{2.6}$$

$$\frac{\partial u_i}{\partial x_i}=0 \tag{2.7}$$

Where u_i is the fluid velocity, p is the pressure, ν is the fluid kinematic viscosity, and body forces do not appear explicitly.

According to the Reynolds decomposition concept, the dependent variables of the system 2.6 and 2.7 are decomposed into mean and fluctuating parts:

$$u_i=\overline{u_i}+u_i', \quad p=\overline{p}+p' \tag{2.8}$$

According to Reynolds decomposition, any instantaneous flow variable (such as velocity or pressure) can be expressed as the sum of its time-averaged (mean) component and a fluctuating component. For example, the velocity component in the i-th direction is written as $u_i=\overline{u}_i+u_i'$, where $\overline{u}_i$ is the mean velocity and u_i' is the turbulent fluctuation. Similarly, the pressure field is decomposed as $p=\overline{p}+p'$, with $\overline{p}$ representing the mean pressure and p' the fluctuating pressure. This decomposition forms the basis for deriving the Reynolds-Averaged Navier-Stokes (RANS) equations, which describe the behavior of turbulent flows in terms of mean quantities.

By substituting equation 2.8 into equations 2.6 and 2.7 and taking into account a few of properties, it is obtained the system of partial differential equations that governs the mean-velocity and pressure fields of incompressible turbulent flow:

$$\frac{\partial \overline{u_i}}{\partial t}+\frac{\partial}{\partial x_j}\left(\overline{u_i u_j}\right)=-\frac{\partial \overline{p}}{\partial x_i}+\nu\frac{\partial^2 \overline{u_i}}{\partial x_j \partial x_j} \tag{2.9}$$

$$\frac{\partial \overline{u_i}}{\partial x_i}=0 \tag{2.10}$$

Using some nonlinear term, it could be obtained the RANS :

$$\frac{\partial \overline{u_i}}{\partial t}+\overline{u_j}\frac{\partial \overline{u_i}}{\partial x_j}=-\frac{\partial \overline{p}}{\partial x_i}+\nu\frac{\partial^2 \overline{u_i}}{\partial x_j \partial x_j}-\frac{\partial \tau_{ij}}{\partial x_j} \tag{2.11}$$

$$\frac{\partial \overline{u_i}}{\partial x_i}=0 \tag{2.12}$$

where in the equation 2.11 the convective term is expressed in nonconservative form, and:

$$\tau_{ij}=\overline{u_i' u_j'} \tag{2.13}$$

The terms of the equations are as follows: $\frac{\partial u_i}{\partial t}$ is the temporal derivative of the mean velocity in the i-direction, $\frac{\partial}{\partial x_j}$ is the spatial derivative of the velocity in the j-direction, u_i and u_i' represent the mean and fluctuating velocity, respectively, in the i-direction, p and p' are the mean and fluctuating pressure, respectively, and τ_{ij} is the turbulent stress tensor, which is calculated as $u_i'u_j'$. These terms are fundamental in the Reynolds-Averaged Navier-Stokes (RANS) equations for modeling turbulent flow and the interaction between the pressure and velocity fields.

2.4 Hybrid Rocket's equations used in post-production

In steady-stage conditions the dynamic of the rocket depends on the total mass flow which is indicated as:

$$\dot{m} = \dot{m}_o + \dot{m}_f = \frac{p_1 A_t}{C^*} \tag{2.14}$$

Where $\dot{m}_o$ is the mass flux of the oxidizer, $\dot{m}_f$ is the mass flux of the fuel, $\dot{m}$ is the mass flux of the hybrid rocket. Moreover, p_1 is the pressure in the first stage, A_t is the area of the throat, and C^* is an indicator of the quality of combustion and it is independent of the nozzle. The thrust can be written as follows:

$$F = (\dot{m}_o + \dot{m}_f) I_{sp} \tag{2.15}$$

Here I_{sp} is the specific impulse. In the problem the thrust is written in different forms as it is a supersonic rocket.

$$F_1 = 120|\dot{m}|u_{exit} \tag{2.16}$$

Where $\dot{m}$ is the total mass flux of the hybrid rocket, and u_{exit} is the exit velocity, which is multiplied by 120 to account for the geometry of the simulation. This adjustment is necessary to accurately reflect the design parameters in the simulation setup which will be presented in the methodology.

$$F_2 = 120|(F_{fuel} + F_{oxidizer} + F_{wall})| \tag{2.17}$$

The force produced by the fuel is denoted as F_{fuel}, while $F_{oxidizer}$ is the force produced by the oxidizer and F_{wall} refers to the force produced by the wall. The thrust is multiplied by 120 due to the geometry of the mesh.

$$F_3 = 120((|\dot{m}|u_{exit}) + (P_{exit} - P_{outlet})A_{exit}) \tag{2.18}$$

The thrust is also multiplied by 120 to account for the geometry. The mass flux, denoted as $\dot{m}$, is the mass flow rate at the nozzle exit and is considered negative due to geometric configurations and computational fluid dynamics (CFD) considerations. u_{exit} represents the outlet velocity, while P_{exit} is the pressure at the nozzle exit. Additionally, P_{outlet} refers to the ambient pressure, and A_{exit} denotes the area of the nozzle at the exit. This setup is crucial for accurately modeling the performance of the hybrid rocket.

The specific impulse shows how much thrust is generated per unit of propellant mass flow per second. It measures how much efficiently the rocket converts propellant into thrust.

$$I_{sp} = \frac{F}{\dot{m} g_o} \tag{2.19}$$

Where the thrust is denoted as F, g_o refers to the gravity and the mass flow rate is related to $\dot{m}$. In addition,the Equation 2.19 can be simplified using the thrust simplified $T = \dot{m}u_x$:

$$I_{sp} = \frac{u_x}{g_o} \tag{2.20}$$

The axial velocity is denoted as u_x and g_o is the Earth gravity. The fuel mass flow rate of can be written as:

$$\dot{m}_f = \rho_f A_b \dot{r} = \rho_{sf} v A_b \tag{2.21}$$

Knowing this formula and solving for the regression rate term, it is possible to calculate the regression rate:

$$\dot{r} = \frac{\rho_f v}{\rho_g} \tag{2.22}$$

Where ρ_f is the density of the fuel in gas state, A_b is the transversal area of the burner, ρ_{sf} is the density of the fuel in solid state and v is the inlet velocity of the fuel.

3 METHODOLOGY

For development of the simulation, some previous step has been done before the CFD simulation. First of all, it has been used ICEM software.

3.1 Mental map of the process

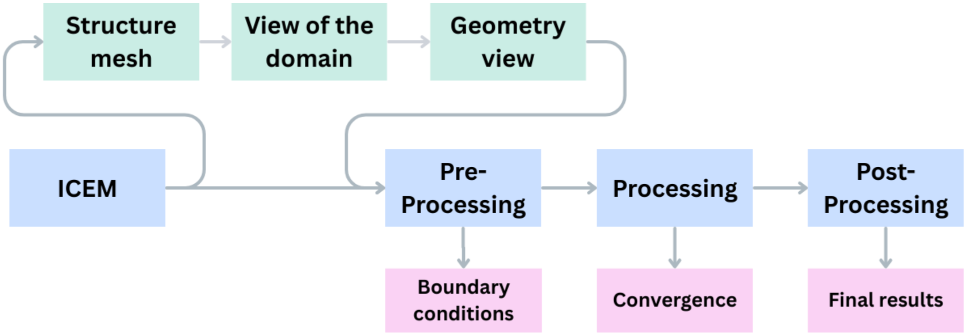

Figure 17 – Mental map of the process

The Figure 17 presents a workflow for a computational simulation process divided into several stages:

1. **ICEM:** This is the initial stage where the geometry, the structural mesh and the domain view are created. The domain is visualized for the simulation setup.
2. **Pre-Processing:** In this phase, the boundary and initial conditions are defined, preparing the system for the simulation to proceed.
3. **Processing:** The simulation calculation takes place here, with constant monitoring of the convergence to ensure accurate results.
4. **Post-Processing:** This stage presents the final results of the simulation after the processing and convergence checks are completed.

The workflow is structured to guide through the key steps of setting up, running, and analyzing a computational simulation, covering both pre-processing, processing, and post-processing phases.

3.2 Integrated Computational Engineering and Manufacturing

The ICEM (Integrated Computational Engineering and Manufacturing) specializes in the generation of geometric meshes for fluid dynamics simulations in CFD. It generates structural and non-structural meshes; additionally, this tool has advanced control over the quality of the mesh and the preparation of complex geometries. Its principal characteristics include advanced tools for hexamedric mesh generation, the possibility of using scripting, advanced visualization of geometry and mesh, and compatibility with different CFD solvers. Figures 18-19-20 show the process of creating the mesh for the hybrid rocket model.

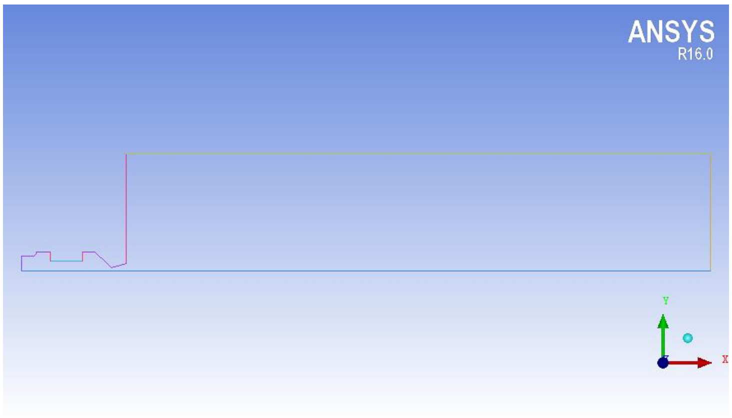

Figure 18 – Geometry

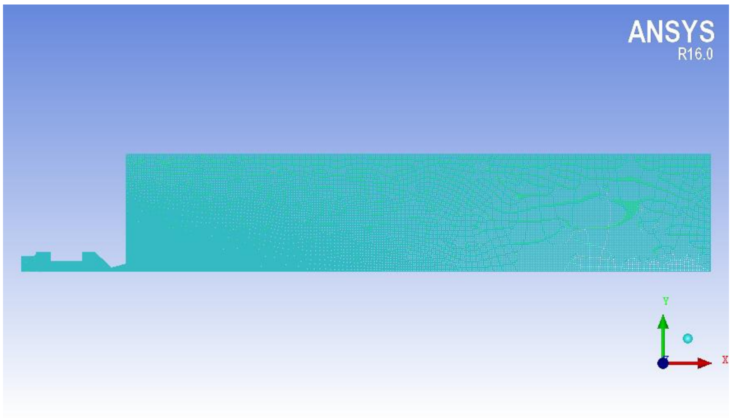

Figure 19 – Mesh

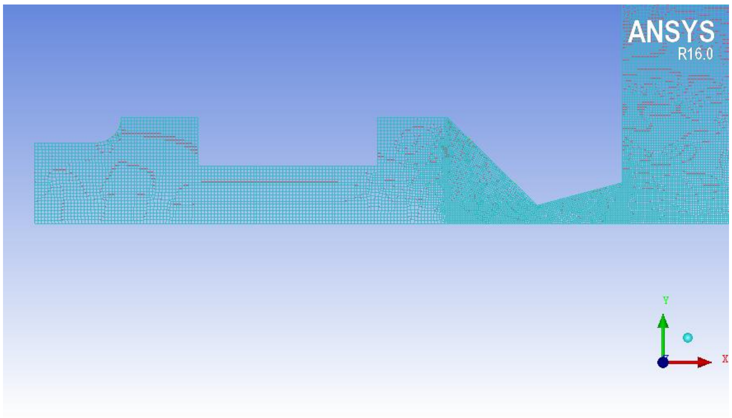

Figure 20 – Mesh zoom

According to Figure 18, which presents a close-up view of the component with a structured mesh, this image illustrates how the hybrid rocket will be simulated. Firstly, it can be observed that the rocket is modeled along a symmetry line. Since rockets are cylindrical, it is not necessary to perform a fully detailed simulation of the entire cylinder. Instead, the model has been simplified by using a 3-degree sector of the cylinder, as shown in Figure 21.

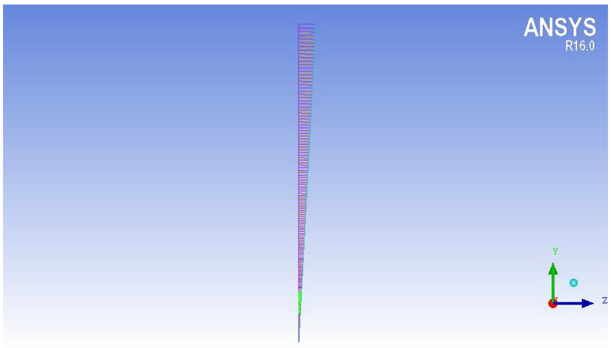

Figure 21 – 3-degree in the mesh

Each color in the figure 18 represents one part of the rocket; for example, the soft blue part corresponds to the fuel in the simulation, and the deep blue part represents the symmetric axis. Moreover, to be specific: deep blue refers to the symmetric axis, soft blue is the fuel section, light red is the front view, deep red is the sides, yellow is the outlet, deep purple is the oxidizer, soft purple is the walls, green is the right side, and pistachio is the top section.

Taking a look at Figure 19, which provides a wider view of the domain, likely including the surrounding medium. In the other Figure 20, only the geometry view appears, without any mesh; just the outline is shown.

3.3 Computational Fluid Dynamic

The simulation workflow includes pre-processing (geometry and meshing), processing (solver execution), and post-processing (results visualization and analysis).

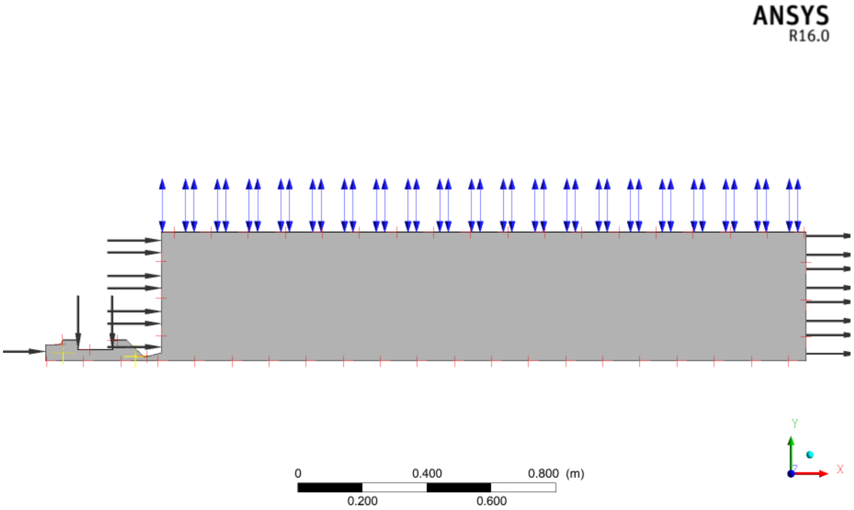

Figure 22 – Pre-processing SARA

3.3.1 Pre-Processing

Figure 22 corresponds to the pre-processing stage of SARA HRM, where the ICEM mesh is imported. Its main tasks are as follows: geometry definition (the rocket mesh), dividing the geometry into finite elements to discretize the domain, defining the fluid properties, establishing boundary conditions, selecting turbulence, heat transfer, and chemical reaction models, setting convergence criteria, time step, and solution methods, and specifying the desired results to be obtained. Figure 23 represents the BOITATÁ hybrid rocket motor, which has differences in geometry compared to the previously mentioned. The choice of boundary and initial conditions is extremely important for obtaining reasonable results and avoiding divergence or fatal errors.

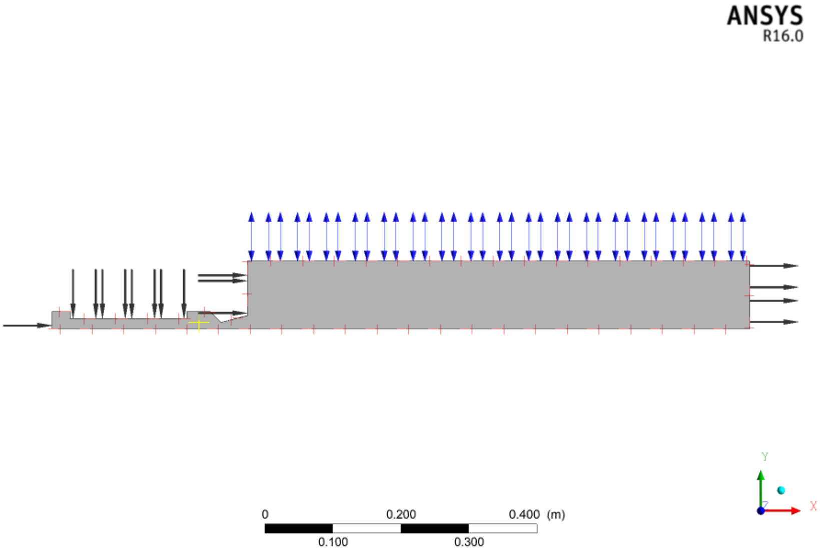

Figure 23 – Pre-processing BOITATÁ

3.3.2 SARA Boundary and initial conditions

For the SARA hybrid rocket, the following boundary conditions are defined in Tables 2-3-4-5-5. The chemical reactions defined are: Nitrous Oxide Air N_2O for the oxidizer, and the fuel is ethylene C_2H_4; the mixture consists of nitrous oxide and ethylene. Before the chemical reactions are included, the materials considered are: air as an ideal gas, air at 25ºC, C_2H_4, C_2H_6, CO_2, gas, N_2, N_2O, soot, water, steel, copper, and aluminum.

Parameter	**Value**
Static Temperature	740 K
Mass Flow Rate $\dot{m}_{fA}$	1.24 $\frac{g}{s}$
Mass Flow Rate $\dot{m}_{fB}$	1.984 $\frac{g}{s}$
Flow regime	Subsonic
Turbulence	Medium

Table 2 – Boundary and initial conditions for the fuel

Parameter	**Value**
Static Temperature	280 K
Mass Flow Rate $\dot{m}_{oA}$	3.22 $\frac{g}{s}$
Mass Flow Rate $\dot{m}_{oB}$	5.152 $\frac{g}{s}$
Flow regime	Subsonic
Turbulence	Medium

Table 3 – Boundary and initial condition for the oxidizer

Parameter	**Value**
Adiabatic Condition	$Q = 0$
Wall roughness	Smooth Wall
No slip wall	$\mu = 0$

Table 4 – Boundary and initial condition for the wall

Parameter	**Value**
Relative Pressure	0 Pa
Opening temperature	290 k

Table 5 – Boundary and initial for the top

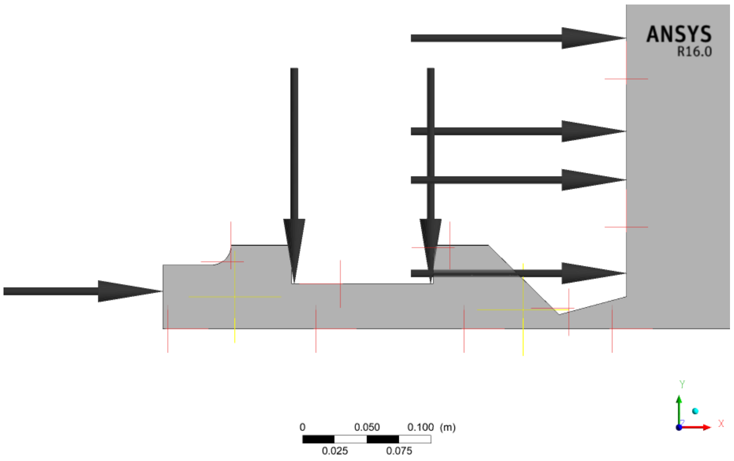

Figure 24 – Zoom in the pre-processing SARA

In Figure 24, two yellow marks can be seen, indicating the maximum temperature and the chamber pressure. The black arrows represent the direction and magnitude of pressure or forces applied to the boundaries of the simulation. In this case, the black arrow on the left is used for the inlet oxidizer, and the vertical arrow in the negative y direction refers to the inlet of the fuel C_2H_4. Moreover, there are a couple of black arrows on the right of Figure 22 that symbolize the outlet of the system.

Finally, the blue arrows, which can also be seen in Figure 22, represent constraints or symmetry conditions and may also indicate displacement restrictions. Knowing the boundary

Parameter	**Value**
Relative Pressure	0 Pa
Static temperature	300 k

Table 6 – Boundary and initial condition for the front

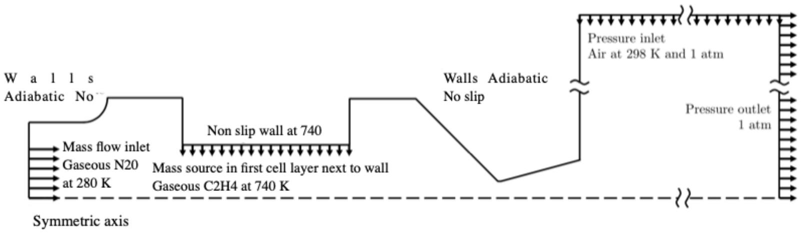

Figure 25 – Hybrid Model 2D

conditions and the geometry of the problem, a simplified scheme of the hybrid rocket can be created.

3.3.3 BOITATÁ Boundary and initial Conditions

For the BOITATÁ boundary and intial conditions, the tables 7-8-9- 10-11 are approximately the same as those used in the SARA hybrid rocket.

Parameter	**Value**
Static Temperature	720 K
Mass Flow Rate $\dot{m}_{fA}$	1.75 $\frac{g}{s}$
Flow regime	Subsonic
Turbulence	Medium

Table 7 – Boundary and initial condition for the fuel

Parameter	**Value**
Static Temperature	289 K
Mass Flow Rate $\dot{m}_{oA}$	2.5 $\frac{g}{s}$
Flow regime	Subsonic
Turbulence	Medium

Table 8 – Boundary and initial condition for the oxidizer

Parameter	**Value**
Adiabatic Condition	$Q = 0$
Wall roughness	Smooth Wall
No slip wall	$\mu = 0$

Table 9 – Boundary and initial condition for the wall

Parameter	**Value**
Relative Pressure	0 Pa
Opening temperature	290 k

Table 10 – Boundary and initial condition for the top

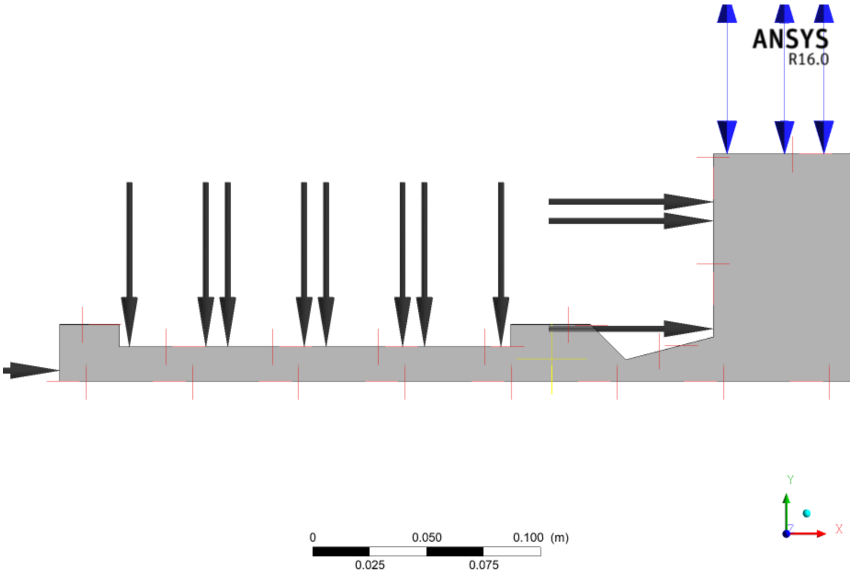

Figure 26 – Zoom in the pre-processing BOITATÁ

As can be seen in figure 26 As can be seen in Figure 26, the dimensions and geometry of this model are different from those of the SARA. This hybrid model is elongated along the x-axis and thinner along the y-axis. The area of the fuel is larger, while the inlet area for the oxidizer is reduced. Figure 27 shows the scheme of the rocket in 2D for simplification.

Parameter	**Value**
Relative Pressure	0 Pa
Static temperature	290 k
Turbulence	Medium
Flow Regime	Subsonic

Table 11 – Boundary and initial condition for the front

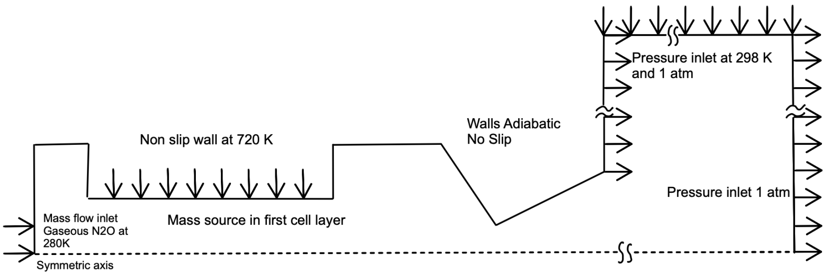

Figure 27 – Hybrid model 2D BOITATA

3.3.4 Processing

Once the pre-processing is complete, including the boundary conditions, the processing stage begins. The simulation is run in this step, and the convergence of the experiment is studied using the time step. It is possible to follow the evolution over time of different values; for example, the pressure or the maximum temperature in the combustion chamber.

3.3.5 Post-Processing

When convergence is reached, the post-processing can begin. Figure 28 illustrates the post-processing stage without any solution, where the results will be represented. In this section, the following aspects can be studied:

- Velocity field: Distribution and magnitude of the fluid velocity throughout the domain.
- Pressure distribution: How the pressure varies inside the fluid and on the walls surfaces.
- Streamlines: Paths followed by fluid particles, showing their direction.
- Turbulence parameters: turbulence kinetic energy and the turbulence of eddy frequency.
- Temperature fields: Thermal distribution and heat transfer.
- Mass fraction: mass fraction of the different reactions.
- Different contour maps.
- Localized parameters: Velocity, pressure, or temperature at critical points.

These solutions depend on the given pre-processing conditions and on the size of the provided time step; the larger the time step, the higher the accuracy of the results. In addition, some of the results can be obtained by performing certain operations using different tools.

Figure 28 – Post-Processing

Among the different tools, *Location>Plane* should be mentioned, which creates a plane at a specific location where particular calculations are analyzed for the general study. This type of plane is located at the outlet of the nozzle 29. Another tool to mention is the *Polyline*, which is found within *Location*. Before using the *Polyline*, the *Location>Isosurface* tool is used to create a surface with a specific variable and value. The *Polyline* corresponds to the intersection between the *Isosurface* and the contour map surface, Figure 30.

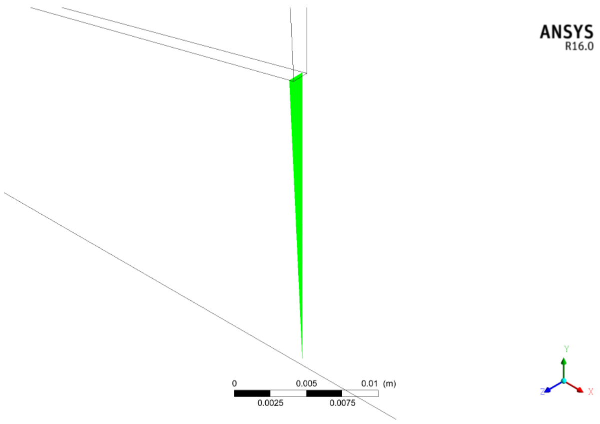

Figure 29 – Outlet plane of the nozzle

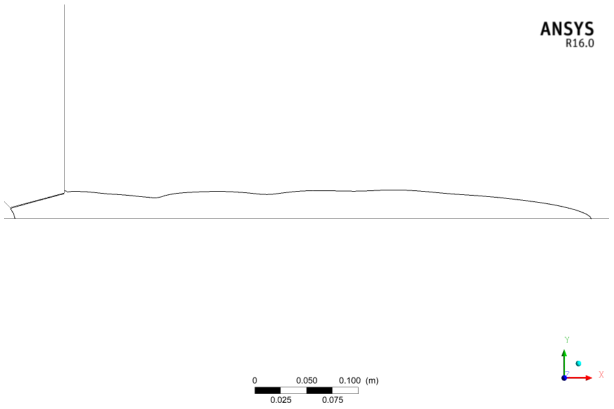

Figure 30 – Example of polyline

To calculate the different values, a combination of two tools is used: first, the *function calculator*, and second, the *Table*.

3.4 Matlab

A simple *Matlab* code is utilized to calculate the regression rate produced in the hybrid rocket propulsion (HPR) system. The data is acquired during the computational fluid dynamics (CFD) post-processing phase, utilizing areas, properties, and tables. This code generates plots that represent the regression rate of the simulation. To calculate the regression curve, the toolbox *Curvefitting* is employed. This tool adjusts curves and surfaces to data in an interactive manner, utilizing both linear and nonlinear regression, interpolation, and data smoothing.

4 RESULTS

The results of the simulation have been divided into different simulations, because different problems had to be addressed to adapt the TOPOS and SARA simulation to the CFD. A maximum pressure of 30 bar in the combustion chamber and a final thrust of 1 kN.

There will be differences between the SARA simulations due to the different maximum mass flow rates for each one, called $\dot{m}_A$ and $\dot{m}_B$. This is because the goal was to achieve 1 kN of thrust at the exit and 30 bar in the combustion chamber in the same simulation. However, it is not possible to meet these conditions in the same experiment with this geometry, so the mass fluxes have been adapted to compare the differences.

With respect to BOITATÁ, a unique simulation was conducted, as the key objective is to achieve 1 kN. Both rockets have been studied with equal importance. The followings figures/models have different scales.

The following results are compared with ()

4.1 Evolution of the Velocity

The velocity simulation is in 2-D, and the Mach number can be seen which is a relation between the velocity and the sound velocity $M = \frac{v}{c}$. The Mach number is fundamental for studying compressible fluxes, especially supersonic and transonic. In the figures below, the throat is choked for all simulations $M = 1$, the gas flow rate is critical in this section as indicated by the equation 1.19.

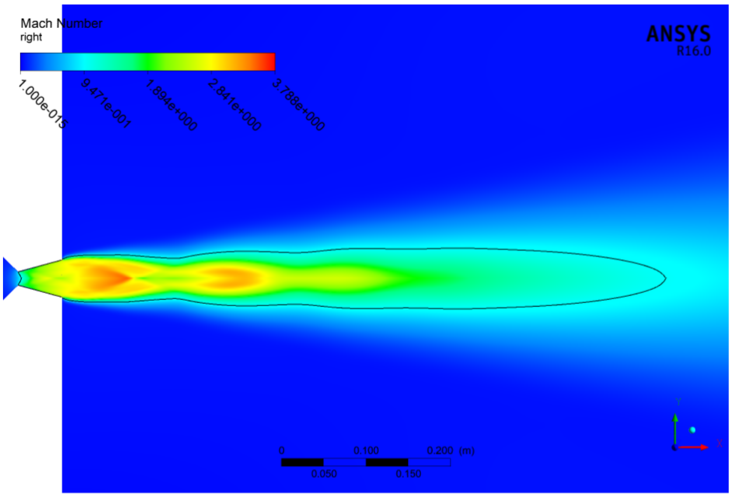

Figure 31 – Evolution Mach for $\dot{m}_A$

In all simulations, M = 1 is localized in the throat; in other words, the nozzle is choked. At the exit of the nozzle it can be seen that velocity increases achieving $M = 3$ for Figures 31,32 and 33. The oblique shock waves are seen for all the experiments outside the nozzle. The Mach

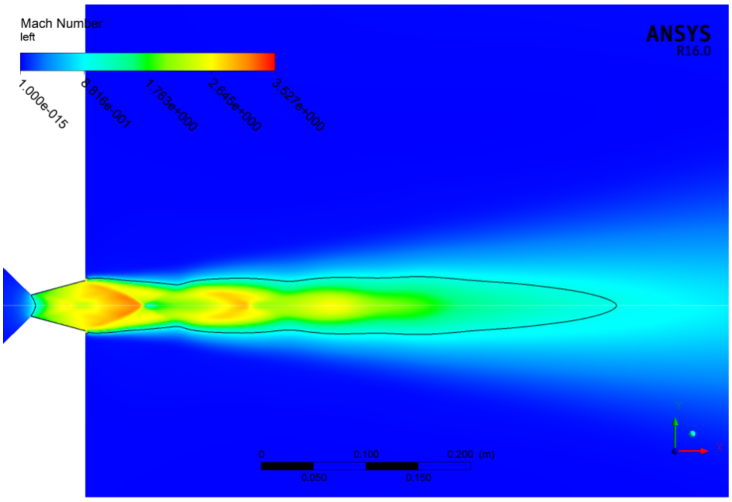

Figure 32 – Evolution Mach for $\dot{m}_B$

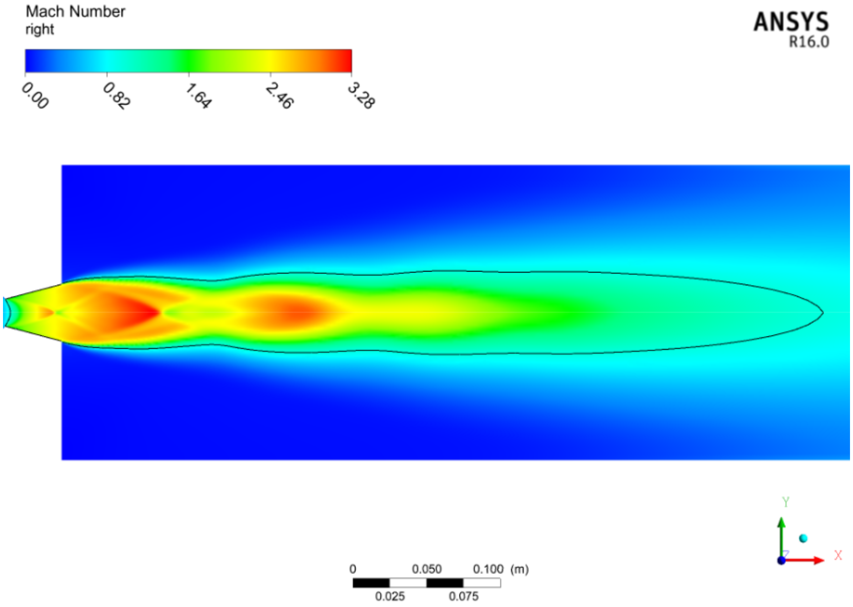

Figure 33 – Evolution Mach for BOITATÁ

diamond is observed where the Mach change is clearly visible in all of the simulations passing from $M = 3$ to $M = 1.7$ approximately, in view of the fact that there exists an oblique shock wave in this part. An acceleration is behind the deceleration, this situation is produced by the Prandtl-Meyer expansion. In addition, inside the nozzle, there is an increase in the Mach number, which also decelerates the flow using a shock wave. This behavior is not common, as is clear in Figure 33.

By analyzing the behavior of the Mach number across all the graphs, it is observed that after reaching its maximum value, there is a smooth deceleration. The Mach disk is not present, so the change in velocity is not abrupt. Another noticeable feature is that the fluid expands into the atmosphere. This response is associated with underexpanded and overexpanded flows, which means that the simulations represent these types of conditions.

In addition, the barrel shock can be identified; in Figure 33, this phenomenon is clearly visible and occurs due to the viscosity of the fluid. Moreover, the slip line is also clearly observed throughout the simulation. Furthermore, it is known that the fluid is composed of a dense gas, as the Mach disk is not as evident compared to that in a dilute gas. Looking at the previously mentioned figure, the Mach structure can be considered moderately underexpanded, as no Mach disk is visible. The flow undergoes Prandtl-Meyer expansion at the nozzle exit, and the rocket exhibits a typical Mach structure.

The black line represents the polyline, the value of the line is M=1. Using this tool, it is more evident that the nozzle is chocked. In Figure 31 the distance traveled M = 1 is smaller than 32.

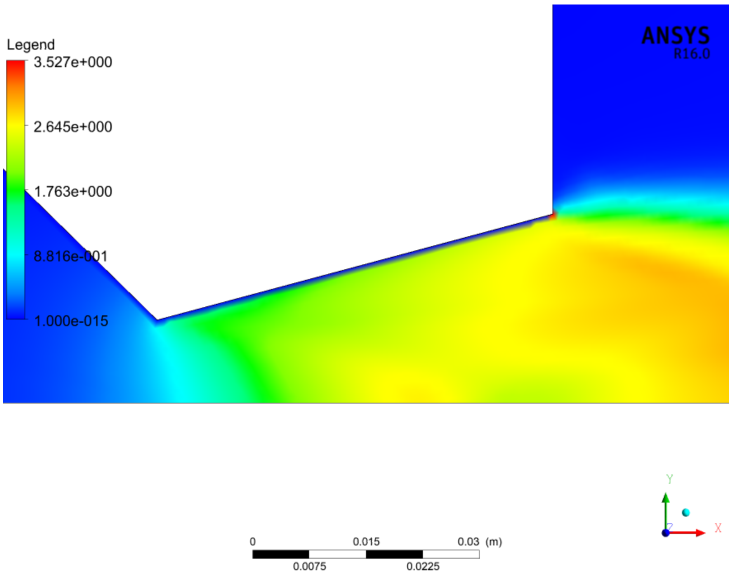

Figure 34 – No slip wall condition

Another relevant point about velocity is shown in Figure 34, which illustrates the no-slip condition at the wall. This condition was defined during the pre-processing stage, and means that the fluid near the wall has the same velocity as the wall. In other words, the fluid at the wall has zero velocity. With this zoom is appreciated the $M = 1$ at the throat which means the flows is choked.

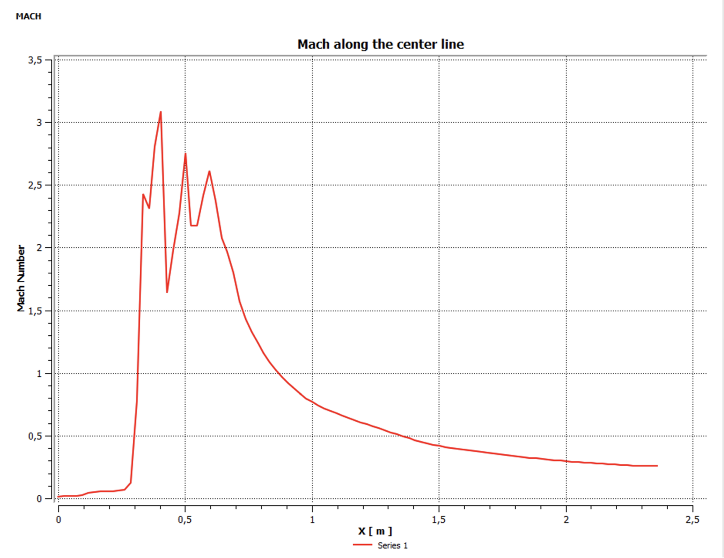

Figure 35 – Mach number along the center line $\dot{m}_A$

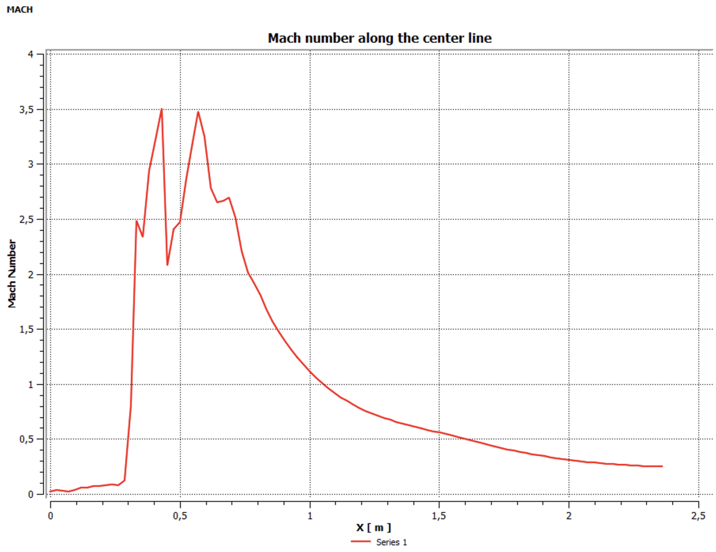

Figure 36 – Mach number along the center line $\dot{m}_B$

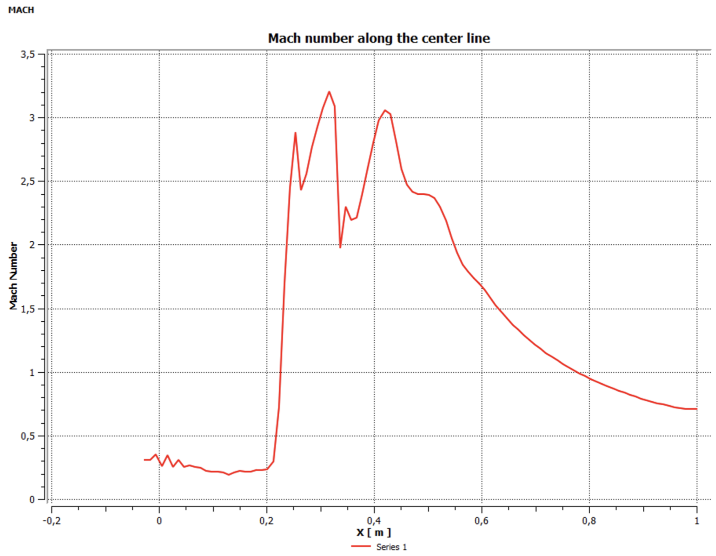

Figure 37 – Mach number along the center line BOITATÁ

In Figure 35,36 and 37, the Mach number along the centerline is shown, demonstrating that the flow is choked in the throat. In addition, the velocity increases due to the Prandtl-Meyer expansions and decreases with the help of shock waves. The acceleration inside the nozzle, along with the deceleration, is clearer when using these graphics.

4.1.1 Vector velocity - Stream lines

The geometry in Figure 38 uses the symmetric axes, as the most relevant information given by the images is the re-circulations produced by the complex geometry of the hybrid rocket.

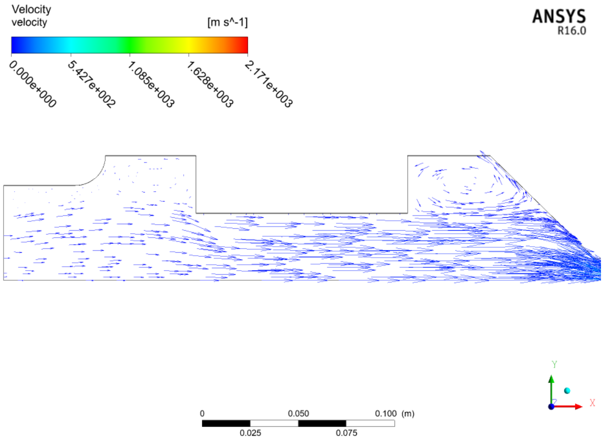

Figure 38 – Vector velocity $\dot{m}_A$

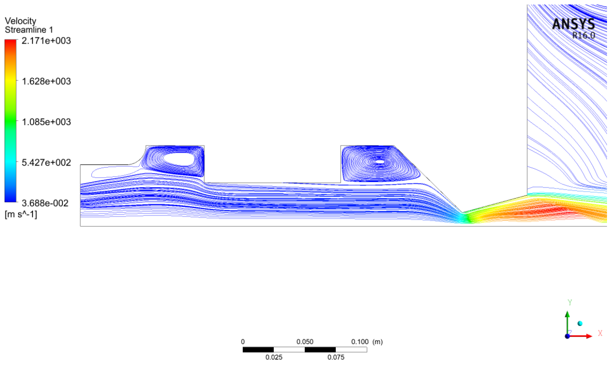

Figure 39 – Streamlines $\dot{m}_A$

The blue arrows represent the velocity of the fluid inside the combustion chamber. There exist two re-circulations inside the simulation, the first one, not so evident as the second one, localized before the fuel inlet in which the flow is affected by the adiabatic wall. The second re-circulation, as the reservoir narrows at the ends by the convergent-divergent nozzle with the oblique adiabatic wall, the flow goes upward and hits the different adiabatic walls. In Figure 39, it can also be appreciated the re-circulations caused by the walls.

4.2 Evolution of the Pressure

Pressure is a key parameter for the success of the mission in rocket motors. Pressure has influence on the thermodynamic efficiency, thrust and structural loading of the walls of the motor to a critical point. If the pressure ratio between the chamber pressure and ambient is sufficiently high, the flow becomes choked. From the pressure graphs below, it can be observed that the ratio $\frac{p_c}{p_a}$ is higher than $\left(\frac{\gamma+1}{2}\right)^{\frac{\gamma}{\gamma-1}}$, which means that the throat is choked, as seen in the previous section.

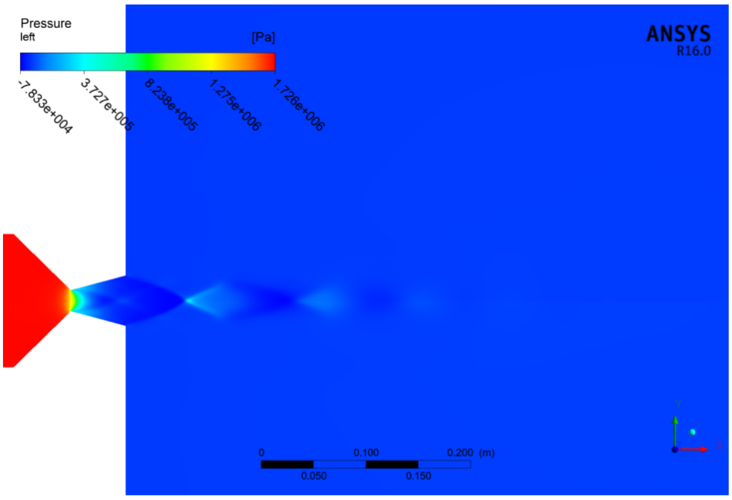

Figure 40 – Evolution Pressure for SARA $P = 17\ bar$ in the combustion chamber $\dot{m}_A$

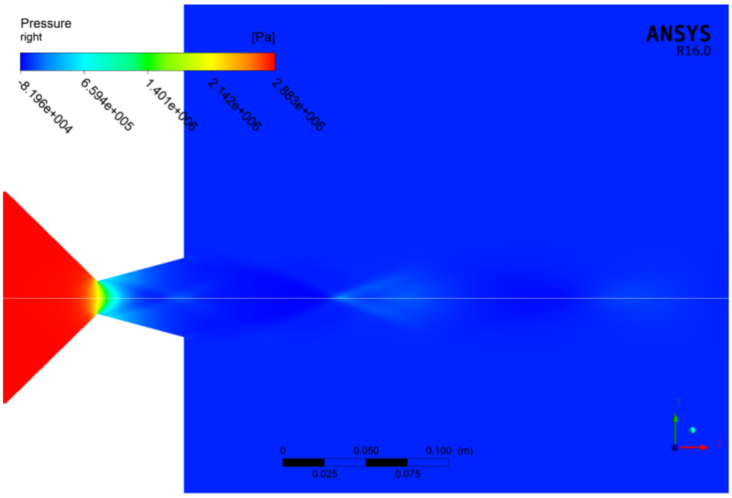

Figure 41 – Evolution Pressure for SARA $P = 30\ bar$ in the combustion chamber, $\dot{m}_B$

The pressure distribution is in 2-D where the red zone represents the highest pressure localized before the throat area, in the combustion chamber or reservoir. At the throat, the pressure decreases. This change in pressure is gradual and not spontaneous in this localization.

In the overexpanded case shown in Figure 40, where the initial conditions are $\dot{m}_A$ and 17 bar in the combustion chamber, the exit pressure is lower than the ambient pressure p_a. This situation generates two shock waves, which in turn produce two additional shock waves that further reduce the velocity, until a Prandtl-Meyer is formed that increases the velocity and reduces the pressure relative to the ambient pressure. It is the case *e* of the Figure 16.

In Figure 41 where the initial condition is $\dot{m}_B$, the outlet pressure is higher than the ambient pressure; therefore, the flow is moderately underexpanded. In Figure 16, the case *g* is the same situation as in this simulation. Although it is not as evident as in the previous case, the Mach diamond can still be identified.

In Figure 40, the diamond structure is more evident because the pressure at the exit is higher than the ambient pressure. Four different diamond structures can be observed. The ambient pressure is introduced between the shock waves separated by the slip line, where in this section it is equal to the ambient pressure. Inside the compression, the pressure difference is higher compared to other simulations.

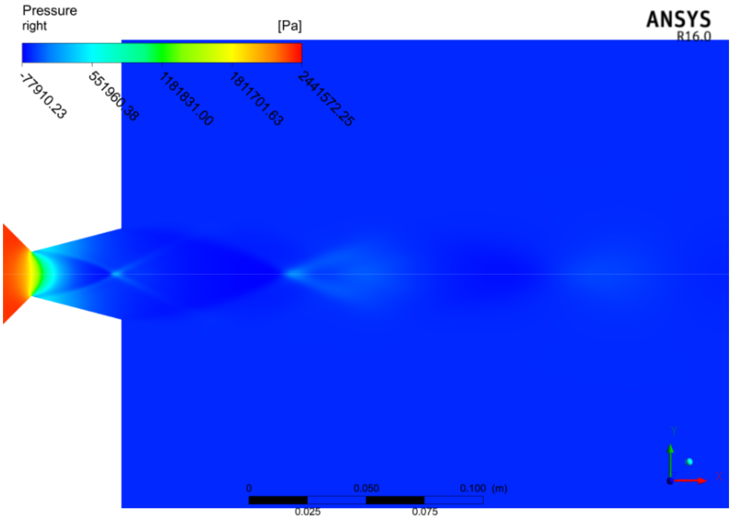

Figure 42 – Evolution Pressure for BOITATÁ

In the BOITATÁ simulation 42, the maximum pressure reached is approximately 24 bar, which is higher than that experienced with 40. At the exhaust, the flow is underexpanded, as shown in Figure 41. The variation of pressure produced by the shock waves and expansion is more significant than in the other underexpanded case. In addition, inside the nozzle, there is a low-pressure regime, lower than the ambient pressure, but it increases its value to reach an underexpanded case using a shock wave.

4.3 Concentration of the oxidizer N_2O

The inlet is where the oxidizer N_2O is introduced, the red color represents the highest concentration of oxidizer. In general terms, this is a contour map in which the orange region is related to the evolution of velocity in the combustion chamber. The orange zone represents the recirculation produced by the crash of the oxidizer mass flux against the adiabatic walls.

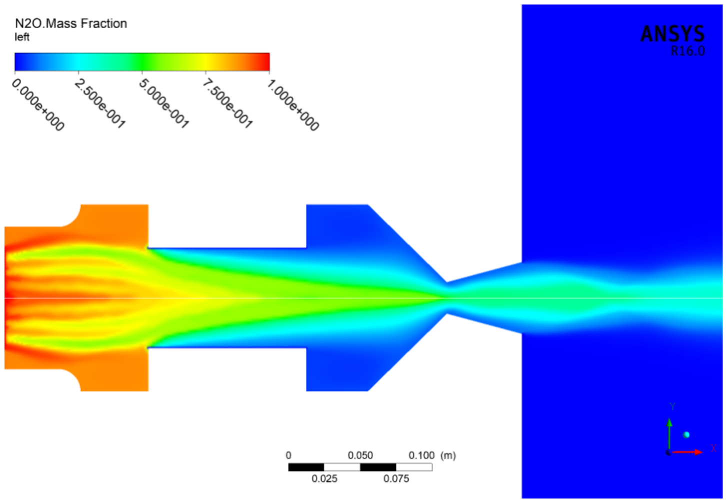

Figure 43 – Concentration evolution of the oxidizer N_2O for $\dot{m}_A$

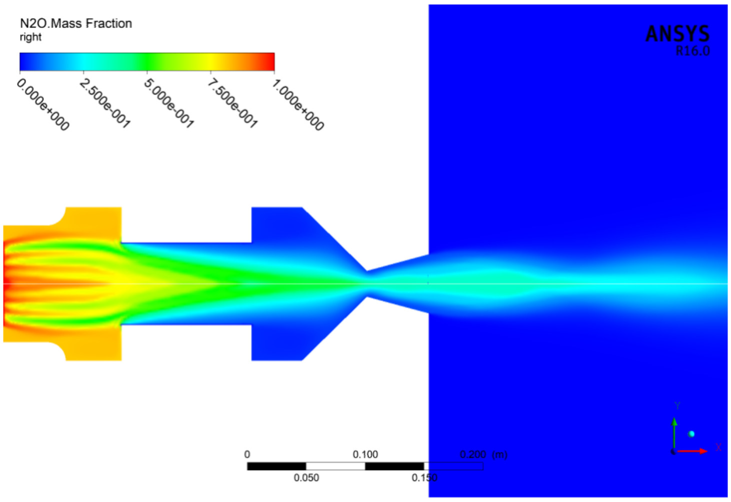

Figure 44 – Concentration evolution of the oxidizer N_2O for $\dot{m}_B$

As the flow progresses in SARA simulation, the concentration of the oxidizer decreases due to dilution with the fuel. When the concentration approaches the fuel region, the boundary layer associated to C_2H_4 can be observed. In this area, both fluids begin to mix. At the beginning of the nozzle, pure oxidizer still exists; in other words, the mixture of oxidizer and fuel is not rich or stoichiometric. At the exit, the oxidizer is mixed with the ambient air, indicating that combustion is not fully completed.

The BOITATÁ simulation 45 presents a less smooth evolution than SARA, however, the oxidizer is fully diluted with ethylene, there is no nitrous oxide in the exhaust. Moreover, the oxidizer concentration is fully diluted with the fuel before reaching the end of the fuel region.

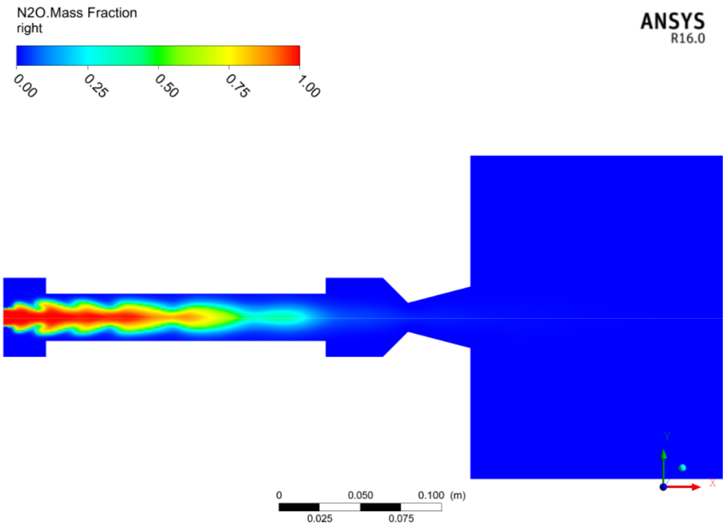

Figure 45 – Concentration evolution of the oxidizer BOITATÁ

The dilution of the oxidizer concentration in Figure 44 is more pronounced than in Figure 43. In Figure 44, a higher amount of $\dot{m}_{oB}$ is injected along with a greater amount of fuel. This is the reason why this figure shows a more significant boundary layer compared to the simulation with $\dot{m}_{oA}$.

4.4 Concentration of the fuel C_2H_4

The red zone in Figures 46-47 is where the fuel C_2H_4 is injected, here the combustion begins as it comes in contact with the oxidizer. As is occurring with the oxidizer and its recirculation, the fuel has his own recirculation that is represented in green in the adiabatic walls. They recirculate the fluid upwards along the oblique wall and become trapped by the other walls as in Figure 38. The boundary layer is more evident with the fuel as a reference compared to the oxidizer 43.

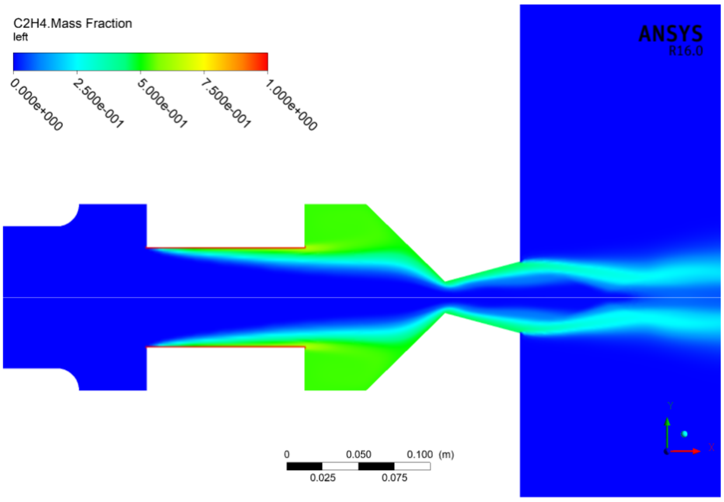

Figure 46 – Concentration evolution of the fuel C_2H_4 for $\dot{m}_A$

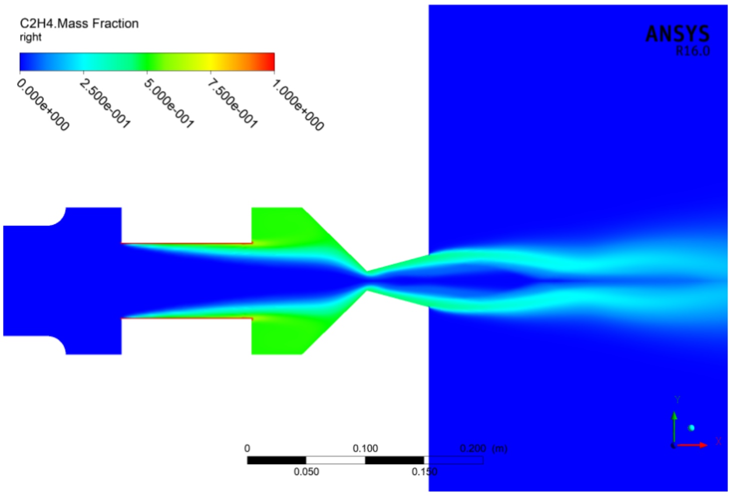

Figure 47 – Concentration evolution of the fuel C_2H_4 for $\dot{m}_B$

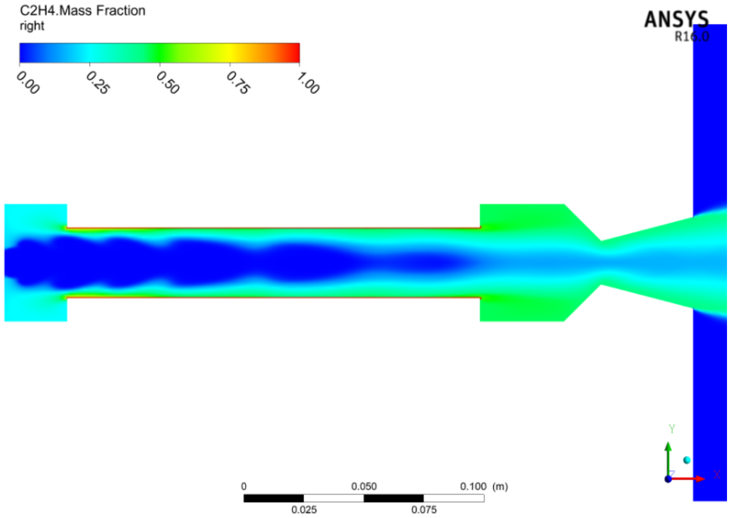

Figure 48 – Concentration evolution of the fuel BOITATÁ

In all simulations, the concentration of C_2H_4 does not completely mix with the oxidizer. At the exit of the nozzle, the fuel mixes with the ambient. In 47 the fuel appears more diluted due to the higher mass fuel rate compared with 46.

In the BOITATÁ 48 case, the fuel is not fully mixed with the oxidizer, resulting in a non-stoichiometric mixture. Part of the fuel flows upward within the combustion chamber, indicating a recirculation zone. Furthermore, another recirculation occurs near the end of the combustion chamber. Finally, a significant amount of unburned fuel exits through the nozzle and mixes with the ambient.

4.5 Temperature of the rocket

The highest temperature is reached where the oxidizer and the fuel mix. This high-temperature region follows the fluid flow until the beginning of the nozzle, where it starts to decline. However, at the end of the nozzle the temperature is still high, these are the flames and gases that are seen at the rockets.

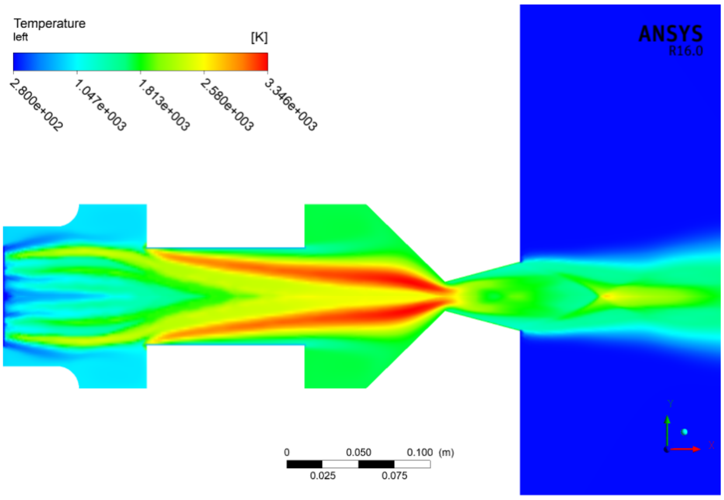

Figure 49 – Temperature of the rocket for $\dot{m}_A$

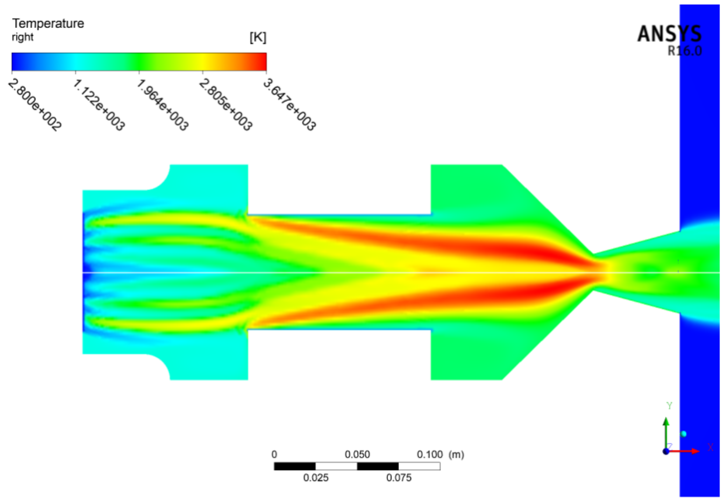

Figure 50 – Temperature of the rocket for $\dot{m}_B$

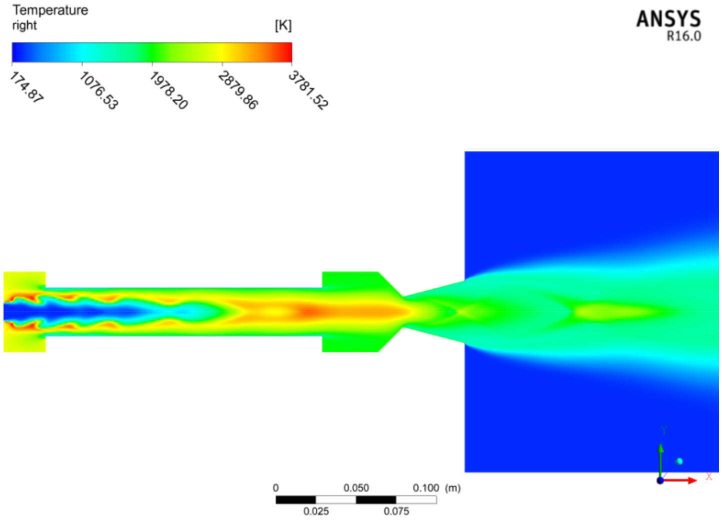

Figure 51 – Temperature of the rocket BOITATÁ

Outside the rocket in Figure 51, an increase in temperature can be observed, caused by the shock wave, and as was described before, the shock wave can also alter thermal properties. Additionally, a decrease of temperature is produced by the Prandtl-Meyer expansion. In both geometries, the highest temperatures do not reach the walls; therefore, there are no structural thermal issues.

4.6 Regression Rate

After getting the data from the simulation, the following *Matlab* code is created to calculate the regression rate.

```
clc
clear all
close all

m_f = 1.24;
m_o = 3.22;

%% REGRESSION RATE
% Using the formula G_0 = a G_0^n

a = 0.0876; %[m^(1+2n) s^(-1+n) kg^-n]

n = 0.3953;% [adimentional]


%% Data from ANSYS

G_ = [7.99e03, 7.411e03, 7.121e03, 6.866e03, 6.514e03, 6.361e03, 6.239e03, ...
    6.040e03, 5.835e03, 5.693e03, 5.556e03, 5.407e03, 5.306e03, 5.160e03,...
    5.035e03, 4.915e03, 4.868e03, 4.751e03, 4.663e03, 4.555e03, 4.452e03 ,...
    4.378e03, 4.301e03, 4.205e03, 4.124e03];%[kg m^-2 s^-1]

x0 = [0.101, 0.105, 0.1075, 0.11, 0.115, 0.1175, 0.12, 0.125,...
    0.13, 0.135, 0.14, 0.145, 0.15, 0.155, 0.16,...
    0.165, 0.17, 0.175, 0.18, 0.185, 0.19, 0.195, 0.2, 0.205, 0.21];%[m]


```

```
%G_0_eng = G_0.* 0.0014223; %[lbm/in^2s] ----- 5 [kg m^-2 s^-1]  0.0014223 = 0.0071115 [lbm/in^2s]
%x_eng = x.* 39.3701; %[in] ----- 1 metro =39,3701 inches
%r_eng = a*G_0.^n; %[in/s]
%r = r_eng.*0.0254; %[m/s] ----- 1 in /s=0,0254 m /s
x = x0*1000;%[mm]
G_0 = G_./1e6;%[kg mm^-2 s^-1]
r = a*G_0.^n;%[mm/s]

% BOITAT
G_1 = [2.144e04, 1.412e04, 1.46e04, 5.029e03, 2.332e03];%[kg m^-2 s^-1]

x01 = [0.00001, 0.043, 0.0086, 0.129, 0.172];%[m]

%G_0_eng = G_0.* 0.0014223; %[lbm/in^2s] ----- 5 [kg m^-2 s^-1]  0.0014223 = 0.0071115 [lbm/in^2s]
%x_eng = x.* 39.3701; %[in] ----- 1 metro =39,3701 inches
%r_eng = a*G_0.^n; %[in/s]
%r = r_eng.*0.0254; %[m/s] ----- 1 in /s=0,0254 m /s
x1 = x01*1000;%[mm]
G_01 = G_1./1e6;%[kg mm^-2 s^-1]
r1 = a*G_01.^n;%[mm/s]
[fitresult, gof] = createFit2(x1, r1)
figure
plot(log(G_1), log(r1), '-')
hold on
plot(log(G_1), log(r1), 'o')
title('Curve regression rate')
xlabel('lnG0')
ylabel('lnr')
legend('Data', 'Function')
grid on


%% Now it is used the aplication CURVE FITTER which has the following function to calculate the power function


function [fitresult, gof] = createFit(x, r)
%CREATEFIT(X,R)
%  Create a fit.
```

```
%
%  Data for 'regression' fit:
%      X Input: x
%      Y Output: r
%  Output:
%      fitresult : a fit object representing the fit.
%      gof : structure with goodness-of fit info.
%
%  See also FIT, CFIT, SFIT.

%  Auto-generated by MATLAB on 10-Jun-2025 15:14:11


%% Fit: 'regression'.
[xData, yData] = prepareCurveData( x, r );

% Set up fittype and options.
ft = fittype( 'power1' );
opts = fitoptions( 'Method', 'NonlinearLeastSquares' );
opts.Display = 'Off';
opts.StartPoint = [0.114885915229785 -0.46706194813246];

% Fit model to data.
[fitresult, gof] = fit( xData, yData, ft, opts );

% Plot fit with data.
figure( 'Name', 'regression' );
h = plot( fitresult, xData, yData );
legend( h, 'r vs. x', 'regression', 'Location', 'NorthEast', 'Interpreter', 'none' );
% Label axes
xlabel( 'x', 'Interpreter', 'none' );
ylabel( 'r', 'Interpreter', 'none' );
grid on

%% Now it is used the aplication CURVE FITTER which has the following function
function [fitresult, gof] = createFit2(x1, r1)
%CREATEFIT(X1,R1)
%  Create a fit.
%
%  Data for 'Regression Rate respect position' fit:
```

```
106 %      X Input: x1
107 %      Y Output: r1
108 %  Output:
109 %      fitresult : a fit object representing the fit.
110 %      gof : structure with goodness-of fit info.
111 %
112 %  See also FIT, CFIT, SFIT.
113
114 %  Auto-generated by MATLAB on 20-Jun-2025 23:31:58
115
116
117 %% Fit: 'Regression Rate respect position'.
118 [xData, yData] = prepareCurveData( x1, r1 );
119
120 % Set up fittype and options.
121 ft = fittype( 'poly3' );
122
123 % Fit model to data.
124 [fitresult, gof] = fit( xData, yData, ft );
125
126 % Plot fit with data.
127 figure( 'Name', 'Regression Rate respect position' );
128 h = plot( fitresult, xData, yData );
129 title('Regression Rate respect position')
130 legend( h, 'Points', 'Function', 'Location', 'NorthEast', '
       Interpreter', 'none' );
131 % Label axes
132 xlabel( 'Position (mm)', 'Interpreter', 'none' );
133 ylabel( 'Regression Rate (mm/s)', 'Interpreter', 'none' );
134 grid on
```

Listing 4.1 – Calculation of the regression rate

As explained above, the approximation proposed by (Liu *et al.*, 2020) to calculate the regression rate is given by $r = 0.087G_o^{0.3953}$. Specifically, from the *line 14* is created the constant *a* which in this case is 0.087 and the *n* is 0.3953. The simulations dimensions correspond to a small laboratory-scale rocket, making the scale appropriate for this analysis. The curve is obtained using *Matlab's Curve Fitter*.

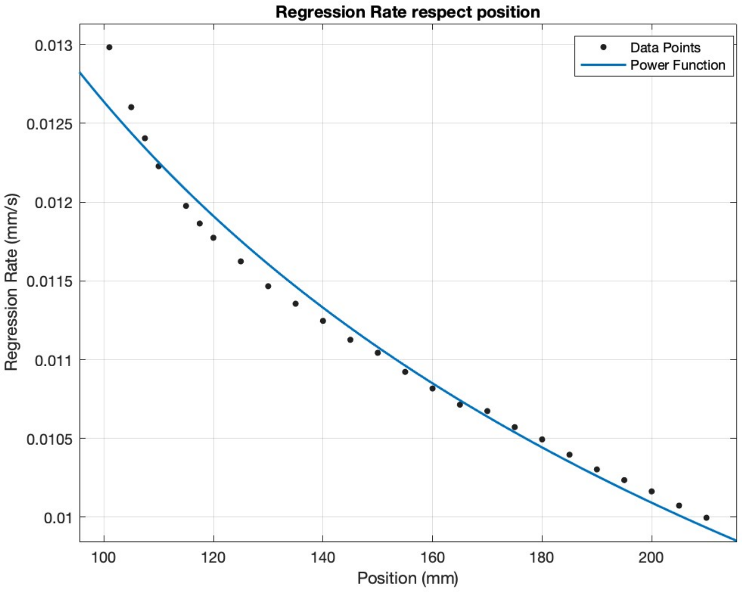

Figure 52 – Regression rate respect position SARA

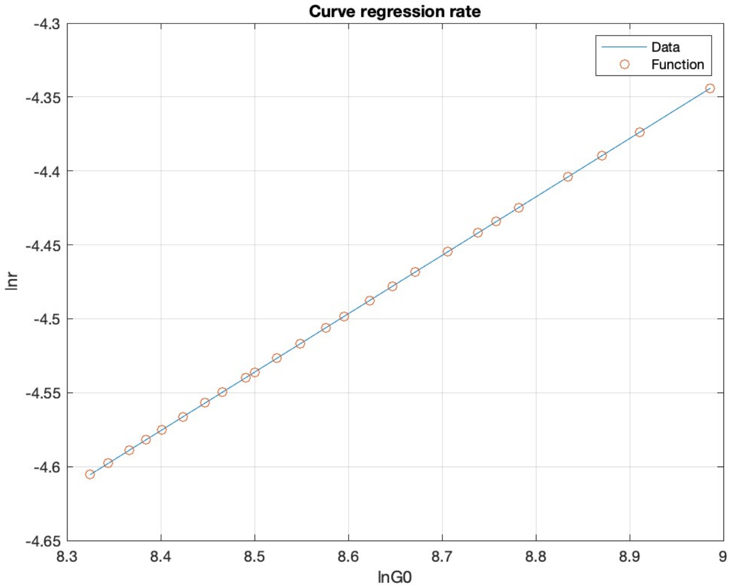

Figure 53 – Curve of regression rate SARA

As shown in Figure 7, the fuel is consumed more rapidly in the first section of the fuel grain, which is expected. Figures 43 and 46 support this observation because in the first section nitrous oxide and ethylene are in constant contact, leading to early fuel consumption compared to downstream sections. In addition, the boundary layer between the fluids serves as another indicator of the regression rate behavior. In Figure 53 shows the regression rate curve in logarithmic form.

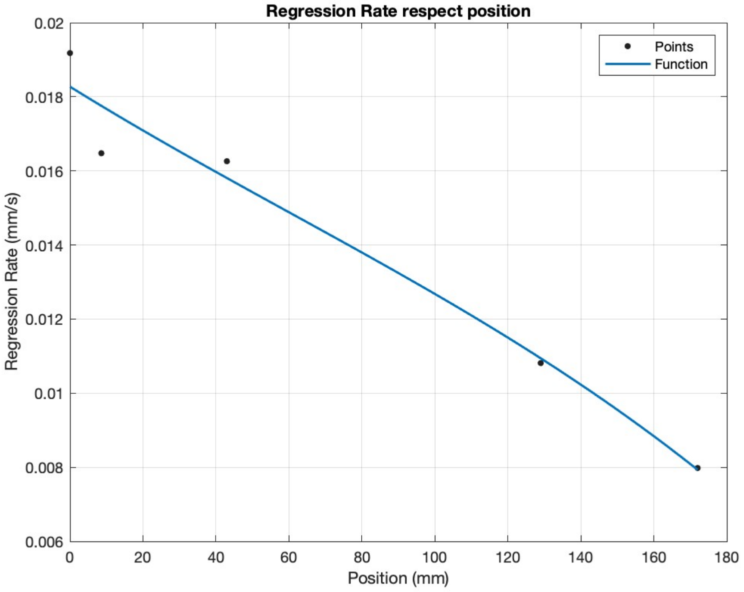

Figure 54 – Regression rate respect position BOITATÁ

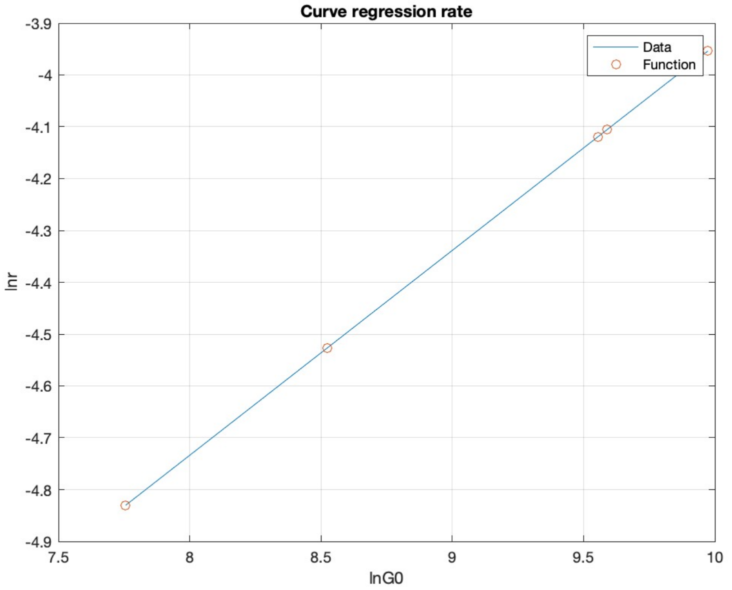

Figure 55 – Curve of regression rate BOITATÁ

The regression rate of the BOITATÁ hybrid model 54 is higher than the SARA simulations. It has the same general behavior as the previous model presented, at the beginning the fuel is consumed more rapidly. However, toward to the end of the fuel surface, the fuel is consumption rate is slower compared to SARA.

The behavior illustrated in previous graph can be observed in Figures 48 and 45, in the first section the fuel is consumed earlier. Controlling the regression rate is challenging as the income fuel mass varies depending on properties of the fluid C_2H_4 such as temperature, pressure, and density.

4.7 Numerical results

To obtain the numerical results, the different functions of *Ansys* as *calculator function, table and surfaces*.

Table 12 – Numerical Results $\dot{m}_A$

Value	**Result**
Thrust 1	985.066 N
Thrust 2	918.202 N
Thrust 3	985.70 N
Specific Impulse	187.7 s
Effective exhaust velocity	1840.86 $\frac{m}{s}$

Table 13 – Numerical Results $\dot{m}_B$

Value	**Result**
Thrust 1	1677.74 N
Thrust 2	1666.11 N
Thrust 3	1678.11 N
Specific Impulse	179.461 s
Effective exhaust velocity	1827.530 $\frac{m}{s}$

Thrust 1 is related to the equation 2.16, Thrust 2 belongs to 2.18 and Thrust 3 to 2.17. Although different formulations are used, the resulting thrust value are approximately the same.

The specific impulse is calculated using equation 2.19 and is practically the same for the both SARA simulations, although is a slightly lower than a typical HRM.

Table 12 refers to the simulation m_A in which 17 bar are achieved in the combustion chamber. While is not the condition originally target by TOPUS, the resulting thrust is close to the intended value.

Table 14 presents the results for simulation m_B, where the pressure in the combustion chamber matches with the TOPUS proposed, however, the resulting thrust is overestimated compared to the initial goal.

Using the real geometry of TOPUS, the following results are obtained:

Table 14 – Numerical Results BOITATÁ

Value	**Result**
Thrust 1	953 N
Thrust 2	941 N
Thrust 3	965 N
Specific Impulse	186.450 s
Effective exhaust velocity	1828.450 $\frac{m}{s}$

These results are more accurate than the SARA model of TOPUS target. The pressure in the combustion chamber reaches the combustion chamber approximately 24 bar and it has a final thrust of 965 N, making the simulation entirely suitable for the mission. It has a usual specific impulse for a hybrid rocket, although it is slightly in the lower side.

5 CONCLUSION

After working with different simulations and models with different types of analysis, trials and errors, and optimizations, several conclusions are obtained.

5.1 Inside the rocket

First of all, during the simulation of how the HRM works over the missions, the only controllable option is the injection of the oxidizer, as it can be kept constant or modified for different situations. This is a characteristic of why hybrid rockets are the safest rockets. The quantity of nitrous oxide injected affects the pressure in the combustion chamber; in other words, an increase in this value will raise the pressure in the reservoir. The same will happen with the temperature of the chamber. Another consequence of increasing N_2O is that the regression rate will be faster because there is more oxidizer available to burn the fuel.

The simulation may fail to converge if the initial and boundary conditions are not set appropriately. Therefore, the importance of choosing these conditions is extremely high to avoid creating a fatal error in a real test. It is crucial to ensure that the initial parameters are adequately defined to achieve reliable results.

The principal difference between the two SARA simulations is the injected oxidizer mass flow. The pressures between the two simulations differ as a result of the injection of the oxidizer. The main consequence of this difference is the thrust, which is higher for $\dot{m}_B$ due to the increased pressure in the combustion chamber. This elevated pressure enhances the energy within the chamber, resulting in an increase in exhaust velocity and, consequently, thrust, as explained in equation 2.16.

Having higher pressure in the combustion chamber will also have a structural implications, to withstand this pressure, the walls of the rocket must be thicker, which will make the structure heavier and more robust. This structural configuration will also have an economical impact, as a greater amount of material will be necessary. If the principal goal is to achieve 1 KN thrust as a limit, the best option will be $\dot{m}_A$, since it requires less pressure in the combustion chamber to meet the mission goal. Moreover, operating at lower pressure(17 bar)allows for a thinner rocket framework, making it potentially cheaper overall.

The fuel mass flow varies according to the initial conditions, and is influenced by the temperature, pressure, and density of the fluids. Therefore, controlling the incoming fuel to achieve stoichiometric combustion or to regulate fuel consumption is a complex task. One potential strategy for better controlling the regression rate is to vary the fuel injection profile. Instead of maintaining a uniform injection along the entire fuel surface, a power-law injection could be implemented-injecting a greater amount of fuel in certain sections than in others. To achieve a hybrid rocket with a low regression rate, it may be optimal to use a non-rich mixture. This approach allows for a situation where either the fuel or oxidizer does not fully mix with the other. Specifically, increasing the inlet quantity of oxidizer while decreasing the fuel mass flow rate can help maintain this balance. By ensuring that there is an ample supply of oxidizer, the combustion process can be more controlled, potentially leading to a more efficient regression rate without compromising performance. This method can help optimize the rocket's efficiency and effectiveness during operation, aligning with the overall mission goals.

The BOITATÁ simulation presents several differences with respect to the SARA simulation, the most notable being the geometry, although the overall rocket dimensions are smaller, the fuel is proportionally larger. The pressure inside the combustion chamber is lower than the target of 30 bar, reaching approximately a 1 kN of thrust. Consequently, the thickness of the structural walls can be reduced, as explained before, it would lower manufacturing costs. Since the rocket is longer compared to the SARA broader structure may pose structural challenges as it has a larger surface and reduced thickness. Although the nitrous oxide is fully mixed with the ethylene, the mixture is not stoichiometric, and an portion of fuel exits the combustion chamber unburned and mixes with the ambient air.

While the simulations exhibit notable differences, they also share similarities, particularly in the recirculation patterns of the fluids within the combustion chamber. In addition, the combustion occurs inside the motor without making contact with the walls which demonstrates excellent behavior.

5.2 Exhaust

The exhaust phase analysis reveals that in simulations with a higher pressure in the combustion chamber, the flow remains underexpanded, leading to characteristic expansions at the nozzle exit. However, the SARA simulation $\dot{m}_A$, exhibited an overexpanded flow. This overexpanded condition decreases the efficiency of the rocket and requires additional power to sustain constant thrust, which consequently leads to a rapid increase in fuel consumption, presenting a considerable drawback in operational contexts.

Furthermore, the flow dynamics within the convergent-divergent nozzle demonstrate unexpected behavior, where flow velocity both accelerates and decelerates. This phenomenon is attributed to two shock waves that alter the flow characteristics, a behavior that is also reflected in the contour maps of pressure and temperature. The formation of a Mach or diamond structure is indicative of the interplay between shock and expansion waves, influenced by the pressure differential between the nozzle exit and ambient conditions.

5.3 Future

Implementing a future optimization to the problem, the injection of the oxidizer could be tested with a rotational feed, this idea could correct the instabilities of the injection in the SARA geometries which are no constant and the behavior of the oxidizer inside the combustion chamber. This idea could also fix the response of the turbulent oxidizer flow of BOITATÁ which is an unusual response.

The benefits of using a hybrid rocket motor are substantial. In the near future, there is potential for space travel for tourism using these types of motors. Therefore, experimental studies of hybrid rocket motors are essential for the future of the aerospace sector and its advancements in technology and safety.

This thesis has been carried out for academic purposes, aiming to help students better understand the behavior of a hybrid rocket motor. It is also intended to support the development of an experimental rocket by assisting in the selection of boundary and initial conditions, as well as providing a detailed analysis.

REFERENCES

ALFONSI, G. Reynolds-averaged navier-stokes equations for turbulence modeling. **Applied Mechanics Reviews**, v. 62, n. 4, p. 040802–1–040802–43, 2009. Available at: https://doi.org/10.1115/1.3124648.

ANSYS Inc. **Ansys Fluent Theory Guide**. Southpointe, PA, Estados Unidos, 2021. Accedido: 2025-05-28. Available at: https://dl.cfdexperts.net/cfd_resources/Ansys_Documentation/Fluent/Ansys_Fluent_Theory_Guide.pdf.

Ansys, Inc. **What is Computational Fluid Dynamics (CFD)?** 2024. Accedido: 2025-05-28. Available at: https://www.ansys.com/simulation-topics/what-is-computational-fluid-dynamics.

Blue Origin. **Blue Origin - For the benefit of Earth**. 2025. Accessed: 2025-06-25. Available at: https://www.blueorigin.com/es-MX.

CAPíTULO, A. del. Combustion of flake aluminum with ptfe in solid and hybrid rockets. *In*: LIBRO, E. del (ed.). **Nano and Micro-Scale Energetic Materials**. Wiley-VCH, 2022. cap. 12. Accedido: 2025-05-28. Available at: https://onlinelibrary.wiley.com/doi/abs/10.1002/9783527835348.ch12.

CONDE, S. P.; MORA, F. A. R. Desarrollo de cohetes híbridos tipo sonda para potenciar la industria aeroespacial en colombia. **Ciencia y Poder Aéreo**, v. 20, n. 1, p. 15–32, 2025. Open Access under CC BY 4.0 License. Available at: https://doi.org/10.18667/cienciaypoderaereo.833.

CORTEGUERA, C. S. **Diseño y Construcción de un Motor Cohete Híbrido**. Madrid, España: [*S.l.: s.n.*], 2013. Proyecto Final de Carrera, Ingeniería Industrial. Available at: http://www.uc3m.es.

DEQUICK, B.; LEFEBVRE, M.; HENDRICK, P. Cfd simulation of a 1kn paraffin-fueled hybrid rocket engine. *In*: AMERICAN INSTITUTE OF AERONAUTICS AND ASTRONAUTICS. **AIAA Propulsion and Energy 2020 Forum**. Virtual Event, 2020. Simulation and experimental comparison of a 1kN hybrid rocket engine with paraffin fuel.

DEQUICK, B.; LEFEBVRE, M.; HENDRICK, P. Sensitivity analysis of a two-phase cfd simulation of a 1 kn paraffin-fueled hybrid rocket motor. **Energies**, MDPI, v. 14, n. 20, p. 6794, 2021. Available at: https://www.mdpi.com/1996-1073/14/20/6794.

FAENZA, M. *et al.* Hybrid rocket motors regression rate prediction through cfd simulations. *In*: UNIVERSITY OF PADUA AND NAMMO RAUFOSS AS. **6th European Conference for Aeronautics and Space Sciences (EUCASS)**. Padova, Italy, 2015. Available from EUCASS Association.

FRANQUET, E. *et al.* Free underexpanded jets in a quiescent medium: A review. **Progress in Aerospace Sciences**, v. 77, p. 25–45, ago. 2015.

GOPALAN, J. Fascinating world of shock waves. **Resonance**, v. 13, n. 8, p. 752–766, 2008. Accedido el 30 de mayo de 2025. Available at: https://www.researchgate.net/publication/226453825_Fascinating_world_of_shock_waves.

GUARDONE, A.; PARSANI, M.; VIGEVANO, L. Numerical simulations of under-expanded nozzle flows of dense gases. *In*: **Proceedings of the XVIII Congresso dell'Associazione Italiana di Meccanica Teorica e Applicata (AIMETA)**. Italia: [*S.l.: s.n.*], 2007. p. 1–9. Presented at AIMETA 2007.

HANDLING Considerations of Nitrous Oxide in Hybrid Rocket Motor Testing. [*S.l.*], Desconocido. Documento PDF proporcionado por el usuario. Available at: nodisponible.

HYPR Space Technologies. **HYPR Space Technologies - Hybrid Rocket Propulsion Systems**. 2025. Accessed: 2025-05-28. Available at: https://hypr-space.com/index.html.

KOPACZ, W. *et al.* Hydrogen peroxide – a promising oxidizer for rocket propulsion and its application in solid rocket propellants. **FirePhysChem**, Xi'an Modern Chemistry Research Institute, v. 2, p. 56–66, 2022. Open access under CC BY-NC-ND license. Available at: https://doi.org/10.1016/j.fpc.2022.03.009.

Learning Heroes. **Tecnología Espacial: ¿Cómo Está Transformando el Mundo?** 2025. Accedido: 2025-05-28. Available at: https://www.learningheroes.com/aprende-sobre-tecnologias-disruptivas/que-es-la-tecnologia-espacial-avances-y-aplicaciones-mas-alla-de-la-tierra.

LECCESE, G.; CAVALLINI, E.; PIZZARELLI, M. State of art and current challenges of the paraffin–based hybrid rocket technology. *In*: AMERICAN INSTITUTE OF AERONAUTICS AND ASTRONAUTICS. **AIAA Propulsion and Energy 2019 Forum**. Indianapolis, IN, 2019. Available at: https://doi.org/10.2514/6.2019-4010.

LIU, L.-l. *et al.* Regression rate of paraffin-based fuels in hybrid rocket motor. **Aerospace Science and Technology**, Elsevier, v. 107, p. 106269, 2020.

MANNING, R. M.; PENLEY, V. L. **A Feasibility Study of a Hybrid Propellant Rocket for Space Applications**. [*S.l.*], 1963. NASA Technical Note D-1882. Available at: https://ntrs.nasa.gov/api/citations/19630039654/downloads/19630039654.pdf.

MEHTA, M. *et al.* Thruster plume surface interactions: Applications for spacecraft landings on planetary bodies. **Journal of Spacecraft and Rockets**, v. 48, n. 4, p. 684–695, 2011. Numerical and experimental investigations of supersonic jet interactions with a flat surface at various atmospheric pressures.

Nammo. **A very different way to launch into space**. 2023. Accessed: 2025-05-28. Available at: https://www.nammo.com/story/a-very-different-way-to-launch-into-space/.

PATERNITI, A. **A CFD Analysis on Hybrid Rocket Engine Using Swirl Injection and Paraffin-based Fuel**. 2024. Dissertação (Master of Science Thesis) — Politecnico di Milano, Scuola di Ingegneria Industriale e dell'Informazione, Milano, Italy, 2024. Available at: https://example.com.

RAMPAZZO, A.; BARATO, F. Modeling and cfd simulation of regression rate in hybrid rocket motors. **Fire**, MDPI, v. 6, p. 100, 2023. Available at: https://www.mdpi.com/2571-6255/6/3/100.

SAVVIDES, A. **Introduction to Circular and Annular Newtonian Couette Flows with Wall Slip Laws**. 2023. Unpublished manuscript. Available at: path_to_your_file.pdf.

SCHMIDLE, N. Virgin galactic's rocket man. **The New Yorker**. Accedido: 2025-05-28. Available at: https://www.newyorker.com/magazine/2018/08/20/virgin-galactics-rocket-man.

Sierra Nevada Corporation. **SNC's Hybrid Rocket Engines Power SpaceShipTwo on its First Powered Flight Test**. 2013. Accessed: 2025-05-28. Available at: https://www.sncorp.com/news-archive/sncs-hybrid-rocket-engines-power-spaceshiptwo-on-its-first-powered-flight-test/.

Sierra Nevada Corporation. **SNC's Hybrid Rocket Technology Once Again Powers the World's First Commercial Space Tourism Vehicle**. 2013. Accessed: 2025-05-28. Available at: https://www.sncorp.com/news-archive/sncs-hybrid-rocket-technology-once-again-powers-the-worlds-first-commercial-space-tourism-vehicle/.

Sierra Nevada Corporation. **SNC Leverages VORTEX® Engine Technology for DARPA's OpFires Program**. 2020. Accessed: 2025-05-28. Available at: https://www.sncorp.com/news-archive/snc-leverages-vortex-engine-technology-for-darpa-s-opfires-program/.

SUTTON, G. P.; BIBLARZ, O. **Rocket Propulsion Elements**. 9th. ed. Hoboken, New Jersey: John Wiley & Sons, Inc., 2017. ISBN 9781118753651. Available at: https://www.wiley.com/en-us/Rocket+Propulsion+Elements%2C+9th+Edition-p-9781118753651.

SáNCHEZ, A. L.; RODRIGUEZ, J. **Fluid Mechanics**. Madrid: Universidad Carlos III de Madrid, 2021. Documento PDF.

TOPUS Projetos Aeroespaciais. **Boitatá**. 2025. Website. Acesso em 16 junho 2025. Available at: https://sites.google.com/view/topusprojetosaeroespaciais/nossos-projetos/boitat%C3%A1?authuser=0.

Virgin Galactic. **Virgin Galactic - The Spaceline for Earth**. 2025. Accessed: 2025-06-25. Available at: https://www.virgingalactic.com/.

WHITE, F. M. **Fluid Mechanics**. 7th. ed. New York: McGraw-Hill, 2011.